Response and resistance to BET bromodomain inhibitors in triple negative breast cancer

Shaokun Shu[#1,2], **Charles Y. Lin**[#1,2], **Housheng Hansen He**[#1,2,3,4,5], **Robert M. Witwicki**[#1,2], **Doris P. Tabassum**[1], **Justin M. Roberts**[1], **Michalina Janiszewska**[1,2], **Sung Jin Huh**[1,2], **Yi Liang**[4], **Jeremy Ryan**[1,2], **Ernest Doherty**[1,6], **Hisham Mohammed**[7], **Hao Guo**[3], **Daniel G. Stover**[1,2], **Muhammad B. Ekram**[1,2], **Jonathan Brown**[1,2], **Clive D'Santos**[7], **Ian E. Krop**[1,2], **Deborah Dillon**[1,8], **Michael McKeown**[1,2], **Christopher Ott**[1,2], **Jun Qi**[1,2], **Min Ni**[1,2], **Prakash K. Rao**[9], **Melissa Duarte**[9], **Shwu-Yuan Wu**[10], **Cheng-Ming Chiang**[10], **Lars Anders**[11], **Richard A. Young**[11], **Eric Winer**[1,2], **Antony Letai**[1,2], **William T. Barry**[2,3], **Jason S. Carroll**[7], **Henry Long**[9], **Myles Brown**[1,2,9], **X. Shirley Liu**[3,9,12], **Clifford A. Meyer**[1,2,3], **James E. Bradner**[1,2,12], and **Kornelia Polyak**[1,2,9,12]

[1]Department of Medical Oncology, Dana-Farber Cancer Institute, Boston, Massachusetts, USA.

[2]Department of Medicine, Brigham and Women's Hospital, and Department of Medicine, Harvard Medical School, Boston, Massachusetts, USA.

[3]Department of Biostatistics and Computational Biology, Dana-Farber Cancer Institute, and Department of Biostatistics, Harvard School of Public Health, Boston, Massachusetts USA.

[4]Princess Margaret Cancer Center/University Health Network, Toronto, Ontario, M5G1L7, Canada.

[5]Department of Medical Biophysics, University of Toronto, Toronto, Ontario, M5G2M9, Canada.

[6]Harvard University, Cambridge, Massachusetts, USA.

[7]Cancer Research UK, Cambridge Institute, University of Cambridge, UK, CB2 0RE.

Correspondence should be addressed to K.P. (; Email: kornelia_polyak@dfci.harvard.edu) or J.B. (; Email: james_bradner@dfci.harvard.edu)

[8]Department of Pathology, Brigham and Women's Hospital, and Department of Pathology, Harvard Medical School, Boston, Massachusetts, USA.

[9]Center for Functional Cancer Epigenetics, Dana-Farber Cancer Institute, Boston, Massachusetts, USA.

[10]Simmons Comprehensive Cancer Center, Departments of Biochemistry and Pharmacology, University of Texas Southwestern Medical Center, Dallas, Texas, USA.

[11]Whitehead Institute for Biomedical Research, Cambridge, Massachusetts, USA.

[12]Broad Institute, Cambridge, Massachusetts, USA.

[#] These authors contributed equally to this work.

Abstract

Triple negative breast cancer (TNBC) is a heterogeneous and clinically aggressive disease for which there is no targeted therapy[1-3]. BET bromodomain inhibitors, which have shown efficacy in several models of cancer[4-6], have not been evaluated in TNBC. These inhibitors displace BET bromodomain proteins such as BRD4 from chromatin by competing with their acetyllysine recognition modules, leading to inhibition of oncogenic transcriptional programs[7-9]. Here we report the preferential sensitivity of TNBCs to BET bromodomain inhibition *in vitro* and *in vivo*, establishing a rationale for clinical investigation and further motivation to understand mechanisms of resistance. In paired cell lines selected for acquired resistance to BET inhibition from previously sensitive TNBCs, we failed to identify gatekeeper mutations, new driver events or drug pump activation. BET-resistant TNBC cells remain dependent on wild-type BRD4, which supports transcription and cell proliferation in a bromodomain-independent manner. Proteomic studies of resistant TNBC identify strong association with MED1 and hyper-phosphorylation of BRD4 attributable to decreased activity of PP2A, identified here as a principal BRD4 serine phosphatase. Together, these studies provide a rationale for BET inhibition in TNBC and present mechanism-based combination strategies to anticipate clinical drug resistance.

To explore non-oncogene addiction to BRD4 in breast cancer, we studied a series of BET bromodomain inhibitors (BBI) across breast cell lines reflecting transcriptionally-defined breast cancer subtypes: luminal, HER2^{+}, and TNBC[2,10] as well as MCF10A and MCF12A basal/mesenchymal immortalized mammary epithelial cells (Supplementary Table 1). Potent inhibitory effects were observed preferentially in TNBC lines, compared to more resistant luminal lines (Fig. 1a). Analysis of potency of drug response and subtype or known driver mutations identified the basal subtype as the only significant association (p=0.0475) (Supplementary Table 1 and D.N.S.). BRD4 dependency was confirmed by RNAi and phenocopied BBI (Extended data Fig. 1a-c). JQ1 or BRD4 knock-down induced growth inhibition resulted in G1 arrest and apoptosis (Extended Data Fig. 1d-g). Expression of factors described to mediate JQ1 effect (MYC) or required for TNBC growth (JAK2/STAT3) showed no clear association with JQ1 sensitivity (Extended Data Fig. 1h and Extended Data Fig. 2a,b). JQ1 treatment of TNBC cells induced significant morphologic changes consistent with induction of senescence confirmed by β-galactosidase staining and luminal

differentiation evidenced by changes in the expression of basal and luminal markers (Extended Data Fig. 2c-d and Fig. 1b).

Extending the translational significance of these findings, we evaluated the ability of JQ1 to inhibit tumor growth in murine TNBC xenografts. Two week treatment efficiently inhibited established tumor growth from SUM159 and MDA-MB-231 lines, and patient-derived primary human TNBC xenografts (Fig. 1c and Extended Data Fig. 2e,f). Down-regulation of BRD4 using two independent TET-inducible shRNAs produced even more pronounced effects leading to complete tumor regression and failure to regrow even after discontinuing doxycycline treatment (Fig. 1c and Extended Data Fig. 2g). Evidence of BBI-induced basal-to-luminal differentiation was confirmed *in vivo* (Extended Data Fig. 2f,h).

Using integrated epigenomic analysis (Supplementary Table 2), we identified the direct transcriptional targets of BBI in TNBC. BBI binding was identified at active promoter and enhancer regions using ChemSeq[11] for biotinylated JQ1 (Bio-JQ1) enrichment and ChIP-seq for acetyl-histone (H3K27ac) and BRD4 enrichment, with the three marks showing near perfect co-localization (Fig. 1d and Extended Data Fig. 3a). BBI efficiently displaced chromatin-bound BRD4 in treated SUM159 (Fig. 1e and Extended Data Fig. 3b) and in SUM149 cells (Extended Data Fig. 3c). To identify biologically relevant, direct targets of BBI in SUM159 and SUM149 cells, we quantified binding of Bio-JQ1 and BRD4 genome-wide and found strong enrichment at 219 and 159 super-enhancers, respectively (SEs; Fig. 1f and Extended Data Fig. 3d and Supplementary Table 3)[8,9,12,13]. TFs with known roles in breast cancer, such as POU5F1B/MYC[14] and HIF1α[15], were evident among top SE-associated genes in both lines. Kinetic effects of JQ1 treatment on gene expression demonstrated preferential SE-associated gene down-regulation (Fig. 1g and Extended Data Fig. 3e,f). Expression changes were observed within 3 hours after JQ1 treatment and, as expected, more genes were significantly down- than up-regulated (Extended Data Fig. 3g-j, and Supplementary Table 4). Unsupervised Metacore[16] analysis of JQ1 affected target pathways revealed down-regulation of regulatory and effector genes in anti-apoptotic and JAK/STAT signaling pathways (Extended Data Fig. 3k). These data support selective disruption of SE-associated genes by JQ1, leading to deregulation of coordinated transcriptional pathways involved in cell proliferation, invasion, and survival.

Dissecting resistance to targeted therapy is critical to elucidate mechanisms of drug and target action, and to suggest approaches to treat or anticipate drug resistance in patients. Therefore, we established BBI-resistant TNBC cell lines by long-term culture of both SUM159 and SUM149 cells in escalating JQ1 doses. Low (0.5 μM) and high (2.0 μM) doses of JQ1 severely impaired proliferation of parental SUM159 and SUM149 lines, reducing viable cells after 6 days (Fig. 2a and Extended Data Fig. 3l). In contrast, JQ1-resistant cells (SUM159R and SUM149R) proliferated linearly, even in high JQ1 doses (20 μM) (Fig. 2a and Extended Data Fig. 3l). BBI-resistance is not attributable to drug export, as MDR1 and other transporters are not transcriptionally up-regulated (Extended Fig. 4a), co-incubation with MDR1 inhibitors (verapamil) had no effect (Extended Data Fig. 4b), and structurally divergent BBIs are equally inactive as JQ1 (Fig. 2b). Further support is provided by the equivalent chromatin engagement of BRD4 in sensitive and resistant cells, demonstrated by ChemSeq with Bio-JQ1 (Extended Data Fig. 4c). Notably, BBI-resistant TNBC cells retain

sensitivity to compounds from orthogonal active drug classes, such as CXCR2 and JAK2 inhibitors[17]; establishing specific resistance to BBIs (Extended Data Fig. 4d). Adaptive drug resistance was not attributable to outgrowth of a minor subpopulation of pre-existing resistant cells, as 10 independent single cell-derived clones showed similar resistance profiles to pooled SUM159R cells (Extended Data Fig. 4e). Similar results were obtained *in vivo*, as SUM159R derived xenografts derived were JQ1 unresponsive (Extended Data Fig. 4f). In all resistant TNBC populations studied, exome sequencing failed to identify alterations in BET bromodomain-encoding genes (e.g., gatekeepers) or known driver genes (parallel pathway activation; Supplementary Table 5).

Absent new genetic alterations, we explored the plausibility of an epigenomic mechanism of resistance. Differential enhancer analysis revealed a significant gain of SEs in resistant SUM159R cells (ChemSeq; Fig. 2c and Supplementary Table 6). The gain of Bio-JQ1 SEs was associated with enrichment for BRD4 binding to these genomic loci (Fig. 2d) and increased transcription of associated genes (Fig. 2e). An upstream/intragenic region of H3k27ac at the BCL-xL locus featured prominently among top gained SEs in SUM159R (Fig. 2f), consistent with increased BCL-xL mRNA and protein expression in resistant cells (Supplementary Table 7, Extended Data Fig. 4g). Functionally, cells with acquired resistance to BBI featured a concordant switch in JQ1 anti-apoptotic response based on dynamic BH3 profiling[18,19] (Extended Data Fig. 4h).

Observing emergent enhancers in resistant cells, we assessed whether BBI-resistant TNBC cells retained non-oncogene addiction to BRD4. Notably, we observed loss of SUM159R cell viability upon BRD4 knockdown (Extended Data Fig. 5,b). Together these studies establish persistence of BRD4 addiction despite resistance to bromodomain inhibition, establishing the plausibility of bromodomain-independent recruitment of BRD4 to enhancers in BBI-resistant TNBCs. To test this hypothesis, we performed BRD4 ChIP-seq on sensitive and resistant cells with and without JQ1. JQ1 neither displaced BRD4 from chromatin in SUM159R (Fig. 2g), nor meaningfully influence epigenome structure by H3K27ac ChIP-seq (Extended Data Fig. 5c-g). Notably, several luminal markers (FOXA1, CD24, and luminal cytokeratins) were elevated in SUM159R cells in cell culture and *in vivo* (Extended Data Fig. 5h,i), supporting a model whereby resistance arises via essential BRD4 recruitment to chromatin in a bromodomain-independent manner. Similar observations were made in SUM149R cells and in TNBC cells inherently resistant to JQ1 (Extended Data Fig. 3h-j; Extended Data Fig. 6a-d), suggesting a general mechanism of epigenomic resistance to BBI.

To disclose potential differences in BRD4-associated complexes between sensitive and resistant SUM159 cells, we performed quantitative proteomics using RIME (rapid immunoprecipitation mass spectrometry of endogenous proteins)[20] with and without JQ1. Analysis of BRD4-associated proteins identified relative enrichment of MED1 and BRD3 in JQ1-treated resistant cells (Fig. 3a, Extended Data Fig. 7, and Supplementary Table 8). BRD4 immunoprecipitation followed by immunoblot for MED1 and BRD3 revealed that JQ1 efficiently displaced BRD4 from MED1 in sensitive cells, but not in resistant cells (Fig. 3b), a result confirmed in SUM149 and BBI-resistant SUM149R, as well as inherently resistant TNBC and luminal lines (Extended Data Fig. 8a). Though elevated BRD3 abundance was observed in SUM159R, increased association of BRD4 and BRD3 was not

confirmed by immunoblot, (Fig. 3b). To assess functionally whether increased recruitment of BRD4 to chromatin by MED1 underlies resistance to JQ1, we expressed an exogenous bromodomain-inactivated mutant (BDmut) with concomitant knock-down of endogenous BRD4 (Extended Data Fig. 8b,c). Downregulation of endogenous BRD4 decreased cell growth both in parental and resistant cells, which was rescued by enforced expression of wild type BRD4 (Fig. 3c). BDmut BRD4 expression failed to rescue parental SUM159 cells, but supported growth of JQ1-resistant SUM159R consistent with an evident bromodomain-independent mechanism of BRD4 recruitment (Fig. 3c). Next, we assessed the sensitivity of cells expressing BDmut BRD4 to JQ1, observing increased sensitivity to JQ1 In parental SUM159 cells exogenously expressing BDmut (Fig. 3d). In contrast, expression of BDmut BRD4 in SUM159R cells rescued the anti-proliferative effect of JQ1 (Fig. 3e), although this could partially be due to the slower growth of BDmut expressing cells. Together, these studies suggest BBI-resistance is associated with increased binding of BRD4 to MED1, in a bromodomain-independent manner unaffected by JQ1.

A recent study reported that the stability and nuclear localization of BRD4 is increased with phosphorylation by casein kinase II (CK2)[21]. To explore the contribution of BRD4 phosphorylation to BBI-resistance, we performed immunoblot analysis in parental and resistant cells and found a marked increase of phospho-BRD4 (pBRD4) in resistant cells (Fig. 4a and Extended Data Fig. 8d). Small-molecule inhibition of CK2 decreased BRD4 phosphorylation in SUM159 and SUM159R cells (Extended Data Fig. 8e). These results imply BRD4 hyperphosphorylation in resistant cells either due to increased phosphorylation by CK2 or, alternatively, to decreased dephosphorylation by an as yet unidentified BRD4 phosphatase. We therefore first analyzed CK2 activity in parental and resistant cells by performing pan-CK2 substrate immunoblots and detected no significant differences in CK2 activity (Extended Data Fig. 8f).

Inactivation of the PP2A phosphatase tumor suppressor gene occurs commonly in breast cancer and is associated with therapy resistance[22]; PP2A also often opposes CK2 function[23],[24]. Thus, we investigated whether PP2A may dephosphorylate BRD4 and whether decreased PP2A activity could lead to BBI-resistance. Downregulation of PP2A catalytic subunit (*PP2CA*) in SUM149 and SUM159 cells led to increased BRD4 phosphorylation, establishing PP2A as a previously unrecognized BRD4 phosphatase (Fig. 4b), further supported by pharmacologic inhibitors of PP2A that showed similar effects (Extended Data Fig. 8g). To strengthen the link between PP2A activity and BBI-resistance, we tested the JQ1 sensitivity of SUM149 cells following the knock-down of PP2A C subunit and determined that downregulation of PP2A decreased JQ1 sensitivity (Fig. 4c). We have collaboratively reported phenothiazine compounds as activators of PP2A enzymatic activity[25]. Thus, we analyzed pBRD4 levels in SUM159R, SUM149R, and other cell lines after short-term treatment with phenothiazine (PTZ) and detected rapid dephosphorylation of BRD4 (Fig. 4d and Extended Data Fig. 8h). Combined treatment with PTZ and JQ1 overcame BBI-resistance in SUM159R cells (Fig. 4e). To investigate the functional role of BRD4 hyperphosphorylation in BBI-resistance, we analyzed whether BRD4 phosphorylation influences MED1 binding. Indeed, SUM159R cells treated with CK2 inhibitor or PTZ both lead to decreased MED1 abundance in BRD4 immunoprecipitations, suggesting that pBRD4 binds MED1 more efficiently than BRD4 (Fig. 4f,g).

To functionally assess the role for BRD4 phosphorylation in BBI-resistance and MED1 binding, we generated BRD4 constructs encoding mutants that cannot be phosphorylated by CK2 (7 serine to alanine substitutions; "7A mutant") or mimic constitutive phosphorylation (7 serine to aspartate substitutions; "7D mutant"). We first assessed the ability of these constructs to rescue effects of endogenous BRD4 knock-down in stable cell lines (Extended Data Fig. 8b,c). We observed expression of both 7D and 7A mutants supporting the growth of both parental SUM159 and JQ1-resistant SUM159R cells (Fig. 3d). Next, we analyzed MED1 binding and subcellular localization of 7A and 7D mutants +/− JQ1. We found that the 7A mutant displays weaker MED1 binding compared to WT BRD4 and completely dissociates after JQ1 whereas the 7D mutant seems to have higher affinity for MED1 that unaffected by JQ1 treatment (Fig. 4h and Extended Fig. 8i). Lastly, we assessed the sensitivity of cells expressing 7A or 7D mutant BRD4 to JQ1. In parental SUM159 cells exogenously expressed 7D mutant BRD4 decreased sensitivity to JQ1 whereas the 7A mutant slightly increased sensitivity (Fig. 4i). In contrast, expression of 7A mutant BRD4 in SUM159R cells restored JQ1 sensitivity whereas the 7D mutant showed a modest decrease. These results strongly support the hypothesis that hyperphosphorylation of BRD4 arises from decreased PP2A activity in BBI resistant cells leading to increased binding of BRD4 to MED1, recruitment to chromatin and decreased responsiveness to bromodomain inhibition.

To explore the clinical relevance of phospho-BRD4 (pBRD4) in BET inhibitor-naive TNBC, we performed immunofluorescence analysis of a tissue microarray (TMA) featuring of 89 patient-derived TNBC specimens. First, we validated the pBRD4 immunofluorescence assay by comparing xenografts derived from SUM159 and SUM159R cell lines and detected significantly higher pBRD4 in SUM159R cells (Extended Data Fig. 9a). We detected strong pBRD4 staining among a subset of TNBCs (Extended Data Fig. 9b,c), and variable staining overall that was not correlated with expression of the androgen receptor (AR) and basal cytokeratins (bCK; Extended Fig. 9d,e) and it was not significantly associated with disease outcomes (Supplementary Table 9 and Extended Data Fig. 9f).

To extend the translational relevance of our findings, we conducted synergy studies of JQ1 with molecules targeting BCL-xL (ABT737), a gained super-enhancer in SUM159R cells, and modulators of BRD4 phosphorylation, the CK2 inhibitor CX-4945 and the PP2A activator perphenazine (PPZ). We observed significant synergy between JQ1 and all three compounds studied (Extended Data Fig. 10), establishing a rationale for combination studies of BBI in TNBC to improve response and to anticipate BBI resistance.

BRD4 inhibition has demonstrated efficacy in disparate models of cancer in a rapidly expanding literature. Despite apparent resistance in the vast majority of tumor types, as we observed here in TNBC, mechanisms of BBI-resistance have not been mechanistically explained. As this research was in review, two studies reported moderate emergent resistance to BBI in murine AML associated phenotypically with a stem-like state and WNT pathway activation[26],[27]. Interestingly, in our study TNBCs with more basal/stem cell-like features and WNT pathway activation are more sensitive to BET inhibition, whereas resistant disease emerges as epigenomic adaptation to a more differentiated luminal phenotype. Our findings of persistent BET bromodomain dependency despite BBI-resistance, as well as pBRD4

staining in resistant disease should be studied in these murine AML models and further in human leukemia.

Integrating approaches in epigenomics, proteomics, and chemical biology, we provide an example of epigenomic drug resistance by an epigenetic mechanism, where in BBI resistant cells, decreased PP2A activity leads to hyperphosphorylated BRD4, which binds more strongly to MED1, facilitating a bromodomain-independent chromatin recruitment mechanism. This research proposes putative combination strategies to anticipate and overcome BBI resistance, including pairing with BCL-xL inhibitors (e.g., ABT-737) or CK2 inhibitors, and guides the development of second-generation BBIs that disrupt BET function via orthogonal biophysical or biochemical actions. More immediately, the robust efficacy observed in pre-clinical models supports the development of BET inhibition in TNBC alone, and in combination with mechanism-based targeted therapies.

METHODS

Cell lines and breast tumor tissues

Breast cell lines were obtained from the ATCC and Dr. Steve Ethier, University of Michigan, Ann Arbor, MI (SUM series). Cells were cultured in media recommended by the provider, their identity was confirmed by STR analysis, and they were regularly tested for mycoplasma. Breast tumor samples were collected using protocols approved by the DF/HCC Institutional Review Board, informed consent was obtained from all patients. Tumors were minced with razor blades and digested with stirring for 3-4 hours at 37°C in DMEM/F12 with 2 mg/mL BSA, 2 mg/mL collagenase type IV, and 2 mg/mL hyaluronidase. After digestion, cells were filtered through 500-micron mesh, washed in DMEM/F12 with 5% FBS, frozen in DMEM/F12 with 5% FBS and 10% DMSO, and stored in liquid nitrogen for subsequent xenograft studies. PDX IDC50 was derived from a primary tumor of highly invasive metaplastic TNBC resistant chemo and radiation therapy leading to the rapid death of the patient. Exome sequencing of the tumor and xenograft identified numerous mutations including heterozygous frameshift mutation in *PTEN* (chr10_89701964-89701964_A) and *CDH1* chr16_67400242-67400242_C). PDX EL-12-58 was derived from a liver metastasis of a heavily pretreated basal-like TNBC, Oncopanel mutation testing identified homozygous mutations in *BRCA2* (p.S1970*), *TP53* (p.I232fs), *TSC2*, *FLT3*, and *ROS1*, and lower frequency mutations in *RAD21, JAK3, ARID1B, ARID1A, KDM6A*.

High-Throughput Screening of BET Bromodomain Inhibitors in breast cell line panel

We tested a panel of compounds (synthesized in the Bradner lab) in 40 human breast cell lines in a 384-well format at 2,000 cells per well using a semi-automated screen essentially as described[5]. Cell viability at 72 hr was evaluated using ATPlite (Perkin Elmer).

Synergy Studies

SUM149, SUM149R, SUM159, and SUM159R cells were seeded in sterile, white, opaque 384-well microtiter plates (Thermo), using an automated dispensing system (BioTek EL406), at 1,000 cells per well in 50 μl of media. Drugs were delivered in DMSO by robotic pin transfer with a JANUS workstation (100 nl) to achieve a matrix of pairwise dose-

response incubations of each compound, each pair having eight replicates. Following 72 hours of incubation, ATP levels were determined for treated cells and vehicle controls (ATPlite, PerkinElmer). Data were normalized to vehicle controls. Combination indices were determined using the median-effect principle of Chou and Talalay[28] (CalcuSyn Software). Isobologram plots were generated with GraphPad Prism software. Points represent paired values of drug concentrations assessed for synergism. The diagonal line signifies drug additivity. Points above the line represent antagonistic drug combinations, and those below the line represent synergistic drug combinations. Synergy assays were performed in triplicates and repeated 2-3 times.

Xenograft assays

For xenograft assays 5-6-weeks old female CrTac:NCr-*Foxn1nu* and NOD.Cg-*Prkdcscid Il2rgtm1Sug*/JicTac mice were purchased from Taconic. Tumors were induced by bilateral orthotopic mammary fat pad injection of 1×10^6 cells in 50% Matrigel (BD Biosciences) in DMEM/F12 or Medium 171 (except for IDC50-X cells, which were injected with 3% FBS and 4 mg/ml collagen gel in Medium 171). Animal experiments were conducted following protocol 11-023 approved by the Dana-Farber Cancer Institute Animal Care and Use Committee. For all the xenograft studies, the sample size of each group (5-10 mice) is indicated in the figures. We performed pilot experiments using a few (5-10) mice/group followed by larger studies if needed to reach statistical significance and repeated experiments to ensure reproducibility. Due to the nature of the performed experiments, no randomization and no blinding was used as it was deemed unfeasible. However, the resulting tumors were analyzed in a blinded manner. Mice were administered JQ1 (50mg/kg, daily), vehicle only (control) for 14 days beginning at day 14 (SUM159), or doxycycline at day 21 (SUM159-shBRD4) after injection. Mice were euthanized and tumors evaluated 28 and 60 days after injection of parental and TET-inducible shBRD4-expressing SUM159 cells into mammary fat pads.

Cellular viability, senescence, MDR, and BH3 profiling assays

Cell viability and growth assays (Fig. 1a, Fig. 2a,b, Fig. 3d,e, Fig. 4c,i, Extended Fig. 1a,b, Extended Fig. 3i, Extended Fig. 4d,e,g,h, Extended Fig. 10), cycle, apoptosis, and MDR assays were performed in triplicates and repeated 2-3 times. For cell proliferation assays, cells were plated at 500 cells per well in 96-well plates and treated the next day with inhibitors, DMSO or doxycycline (500ng). Cells were cultured at 37°C with 5% CO2 in the media described-above, and cell viability was measured using CellTiter-Glo three days after treatments. For cell growth assays, cells were plated at 5000 (SUM159) or 20000 (SUM149) cells per well in 6-well plates and treated the next day with inhibitors. Cells were counted every three days by cell counter. Cellular apoptosis was analyzed with an APC AnnexinV/ 7ADD Apoptosis Detection kit (BD Pharmingen). AnnexinV/7AAD assessments and cell cycle graphics were generated using FlowJo software V7.6.1 for Windows (Tree Star). Senescence Beta-gal staining was performed using Senescence β-Galactosidase staining kit from Cell signaling. Briefly, after JQ1 treatment (500nM) for 72h, SUM159 and MDA-MB-231 cells were fixed by Fixative Solution for 15 min, followed by β-Galactosidase solution incubation overnight at 37 °C. The staining was checked under microscope for the development of blue color. Multi-Drug Resistance Assay was performed with MDR assay

kit from Cayman Chemical (600370). Briefly, SUM159 and SUM159R cells were treated with JQ1 or DMSO for 30 min in SUM medium. Verapamil was used as a positive control at 1:1000 dilution. Calcein AM/Hoechst Dye staining solution was added after that and cells were incubated at 37 °C for 15 min. The cells were analyzed by fluorescent microscope and FACS. Cell cycle analysis was performed 72 hr after JQ1 treatment or BRD4 downregulation with doxycycline using propidium iodide (PI) staining. Cells were resuspended in 1 ml of growth medium supplemented with 2 μg/ml PI (Life Technologies) as final concentration. After 60 min at 37°C in the dark, analysis was performed on a FACS AriaII cytometer (BD Biosciences). The cell cycle was plotted as histogram after excluding doublets. Cell synchronization Procedure. SUM159 cells were treated with nocodazole (200ng/ml) for 12h and then cells were tapped to detach from the plates. After washing twice with PBS, cells were replated with or without JQ1 in collagen coated plates. Cells were collected at 0, 3, 6, 12 h time point for FACS and immunoblot analysis. Dynamic BH3 profiling was performed using the JC-1 plate method as previously described[18,19]. Briefly, 2.5×10^5 cells were seeded in T25 flasks in the presence of 500 nM or 5 μM JQ1 for 72 or 96 hours. Cells were trypsinized, suspended in MEB (150 mM mannitol, 10 mM HEPES, 50 mM KCl, 5 mM succinate, 20 μM EGTA, 20 μM EGTA, 0.1% protease-free BSA, pH 7.5 +/− 0.1), and $1\text{-}2 \times 10^4$ cells were added in 15 μL of MEB to each well of a 384 well Fluotrac 200 plate containing 15 μL/well of either peptides at 2X final concentration, buffer only, or 50 μM alamethicin in MEB supplemented with 2μ JC-1, 10 mM 2-mercaptoethanol, 20 μg/mL oligomycin, and 50 μg/mL digitonin. Fluorescence at Em 590 +/− nm and Ex 545 +/− 10 nm was recorded at 5 min intervals at 32°C. The area under each curve was normalized to the alamethicin and buffer controls as:

$$\% \text{ Depolarization} = 1 - [(AUC_{sample} - AUC_{alamethicin}) / (AUC_{buffer} - AUC_{alamethicin})].$$

Delta priming was calculated per peptide treatment as: Delta Priming = (Depolarization Treated) − (Depolarization Untreated). Positive delta priming indicates an increase in priming due to treatment and an increased potential for apoptosis at later time points.

Immunofluorescence staining and image and statistical analysis of tissue microarrays

Antibodies used for immunofluorescence were CK18 (Dako, M7010), CK17 (Dako, M7046), HMW CK (Dako, M0630), LMW CK (Dako, M0631), CD44 (NeoMarkers, MS-668-P1), CD24 (NeoMarkers, MS-1279-P1), p-STAT3 (Cell Signaling, 9145S), VIM (Dako, M073501), CDH1 (BD Biosciences, 610181), FLAG (Sigma, F1804), BrdU (Roche, 11170376001), pBRD4 (a gift from Dr. Chiang at University of Texas Southwestern Medical Center), and AR (Cell Signaling, 5153S). Immunofluorescence experiments were performed in cultured cells or in whole sections of formalin-fixed paraffin embedded (FFPE) xenograft tumors. The staining was performed as described[29]. Antibody dilutions were as follows: p-STAT3 (1:25), CD44 (1:100), CD24 (1:100), CK18 (1:200), CK17 (1:200), HMW CK (1:100), LMW CK (1:100), VIM (1:100), CDH1 (1:100), FLAG (1:50), BrdU (1:200), pBRD4 (1:200), and AR (1:50). The Dana-Farber Breast Cancer Tissue Microarray (TMA) consists of primary TNBC samples from approximately 83 patients who underwent definitive breast surgery at Brigham and Women's Hospital between 1/1/1997 to 12/31/2005. Formalin-fixed, paraffin-embedded breast cancers were collected from the archives of the Department of Pathology at Brigham and Women's Hospital. Best blocks and best areas for

coring were identified and selected by a breast pathologist (DD) to represent different area of the tumor. Results of immunohistochemical studies for estrogen (ER) and progesterone receptor (PR) and HER2 and FISH assay results for HER2 were extracted from pathology reports. TMA construction was carried out in the Dana-Farber/Harvard Cancer Center Tissue Microarray Core Facility. Three 0.6 mm cores were taken from different marked areas in each case and placed into a recipient block using a manual arrayer (Beecher Instruments). Specimens are arrayed in triplicate. Participants signed consent for research use of tissue and the linking of tumor specimens to clinical follow-up. Clinical data on these patients was collected retrospectively at first presentation, at 4, 9, 18, 30, and 42 months, and annually thereafter. After 9.3 years median follow up, 24 recurrences and 14 deaths have been recorded. The data elements are the following: staging, tumor pathology, diagnostic and follow-up tests performed, treatments administered (surgery, radiation and systemic therapy), and recurrence. Although the patients in this cohort were not treated as part of a clinical trial protocol, they were treated relatively uniformly as per Dana-Farber clinical practice guidelines. This serves to minimize confounding due to treatment heterogeneity. The TMA was stained with pBRD4 (1:200) antibody and imaged manually on Yokagawa spinning disc confocal microscope. Three images were taken per each core for 240 out of 267 cores, for the remaining 27 one or two images were taken due to tissue loss or low tumor content. Image analysis was performed with ImageJ software macro (code available upon request). Phospho-BRD4 staining mean intensity was calculated per individual nucleus within an image. The mean intensity per image was normalized to nuclei count. For clinical outcome analysis patients were dichotomized as 'High'/'Low' pBRD4 by median intensity (Supplementary Table 9). Disease outcomes were evaluated in 83 of 89 TMA samples (3 were not TNBC by definitive pathology, 2 did not have clinical data available, one was a repeat biopsy on a patient). Recurrence-free survival (RFS) was defined as the interval from the date of initial surgical resection to the date of recurrence (local or distant), or date of last known contact if the patient was alive and has not recurred. RFS and overall survival were estimated using the Kaplan-Meier product-limit method, with hazard ratios and 95% confidence intervals from a univariate Cox proportional hazard model.

siRNAs and lentiviral shRNA and expression constructs

For siRNA transfection cells were plated at 2,000 cells per well in 96-well plates and cultured at 37°C with 5% CO2 in the media. The next day, cells were transfected in triplicate with siGENOME SMARTpools for the genes of interest or "Non-Targeting siRNA" controls using DharmaFECT 1 (Dharmacon). The sequences of the siRNAs in the SMARTpools are listed in Supplementary Table 10. Cell viability was measured using CellTiter-Glo (Promega) three days after transfections, with the effects of each siRNAs treatment on each cell line compared to the effects of no siRNAs.

TET-inducible pLKO-TET-ON lentiviral constructs were packaged by co-transfection of the lentiviral hairpin containing plasmid PLKO.1 and the helper plasmids pCMV-dR8.91 and pMD2.G-VS.V-G into HEK293T cells using Lipofectamin (Life Technolgies). Following transduction via spinoculation for 30 min hr at 1000 g and selection with 1 μg/ml puromycin for 72 hr (Sigma, St. Louis, MO), knockdown efficacy was determined by western blotting

and cells were seeded for proliferation assays as described above. Sequences of shRNAs used are listed in Supplementary Table 10.

Full length BRD4 in pCDNA3 was a gift from Dr. French at Brigham and Women's Hospital, Harvard Medical School. Mutations of BRD4 BD1 (N140A) and BD2 (N433A) bromodomains, 7A and 7D mutants were generated using a Quickchange Multi Site-Directed Mutagenesis Kit (Agilent Technologies) using primers listed in Supplementary Table 10 and subsequently verified by sequencing.

Immunoblotting and immunoprecipitation experiments

Cells were lysed five days after transfection with siRNAs in RIPA buffer. Proteins were resolved in SDS-polyacrylamide gels (4%–12%) and transferred to PVDF membranes by using a Tris-glycine buffer system. Membranes were blocked with 5%milk powder in 0.1% Tween20 in PBS (PBS-T) for 1 hr at room temperature followed by incubation with primary antibodies at 1:1000 dilution in 2.5% milk PBS-T. For immunoprecipitation, nuclear extracts were prepared as follow: 10×10^6 cells were resupended in 5ml Buffer A: 10mM Tris pH 7.9, 1.5mM MgCl2, 10mM KCl, 0.05% NP-40, 1mM DTT, and protease and phosphatase inhibitors. Cells were incubated on ice for 15 min and gently vortexed every 5 min. After centrifugation at 2,000g for 5 min, pellets were suspended in 0.3 ml buffer B (20mM Tris pH 7.9, 25% glycerol, 0.42 M NaCl, 1.5mM MgCl2, 1mM KCl, 0.5% NP40, 0.2mM EDTA, 1mM DTT, and protease and phosphatase inhibitors) and incubated for 5 min on ice. After centrifugation of the lysates at 14g for 10 min at 4°C, supernatant was diluted with 0.6 ml buffer A, and added NP-40 to final 0.5% and treated with DNase I. The samples were then incubated at 4°C overnight with BRD4 or Flag antibodies at 1:100 dilution and immunoprecipitates were collected on Dynabeads Protein G for 2 hr. Beads were washed with buffer B containing 150mM NaCl and 0.5% NP-40 three times and then resuspended in gel loading buffer. Immunoblotting and immunoprecipitation experiments were repeated 2-3 times.

Antibodies and Inhibitors

Antibodies used for immunoblotting, immunoprecipitation and ChIp-seq were as follows: BRD4 (Bethyl, A301-985A), MED1 (Bethyl, A300-793a), BRD3 (Bethyl, A302-368A), BRD2 (Bethyl, A302-583A), MYC (Santa Cruz, sc764), p-STAT3 (Cell Signaling, 9145S), STAT3 (Cell Signaling, 4904), p-STAT5 (Cell Signaling, 9351), p-JAK2 (Cell Signaling, 3771), CYCLIN D1 (Cell Signaling, 2922), p-H3 (Cell Signaling, 12201), CK2 substrate (Cell signaling, 8738), PP2A-A (Cell signaling, 2039), PP2A-C (Cell signaling, 2038) and p-BRD4 was a gift from Dr. Chiang at University of Texas Southwestern Medical Center. Antibodies used for ChIP-seq were BRD4 (Bethyl) Histone H3K27ac (Abcam, ab4729). CXCR2 inhibitor (239819) and CK2 inhibitor (218860) were from CalBiochem, JAK2 inhibitor (INC424), MEK inhibitor (GSK1120212, S2673) and PI3K inhibitor (BKM120, S2247) were from Selleckchem, Phenothiazine (1525707) and perphenazine (1511000) was from Sigma, ABT-737 (s1002) was from Selleckchem. Inhibitor treatment for immunoblot analyses was conducted for 3 hrs.

SILAC-RIME Experiments and data analysis

SUM159 and SUM159R cells were grown in R/K-deficient SILAC DMEM (paa; E15-086), 10% dialyzed serum (Sigma-Aldrich; F0392), and supplemented with 800 μM L-Lysine $^{13}C_6^{15}N_2$Hydrochloride and 482 μM L-Arginine$^{13}C_6^{15}N_4$ hydrochloride (Cambridge Isotope lab) for "heavy"-labeled media or 800 μM L-Lysine $^{12}C_6^{14}N_2$-Hydrochloride and 482 μM L-Arginine $^{12}C_6^{14}N_4$ hydrochloride for "light"-labeled media. After SILAC labeling, RIME was performed as described[20]. Word clouds for Fig. 5a were generated using R version 3.1.0 and the R package "wordcloud" version 2.5. The size of the tag reflects the square root of the MASCOT score of the protein (the choice of square root is arbitrary, but visually appealing). Experiments were filtered against the Contaminant Repository for Affinity Purification Mass Spectrometry Data[30], considering any protein which occurs in at least 20 negative control experiments to be contamination, hence removed from the data set. Refseq protein IDs provided by the contaminant repository were converted to Uniprot IDs found in the mass spec experiments using mappings from the Bioconductor package "org.Hs.eg.db", version 2.14 (Carlson M. org.Hs.eg.db: Genome wide annotation for Human. R package version 3.0.0). SILAC RIME experiments were performed in duplicates and repeated 2-3 times.

In vitro Chem-seq, ChIP-seq, and RNA-seq

Chem-seq was performed essentially as described[11]. ChIP-seq: SUM159 and SUM159R cells (4×10^7) were grown in SUM Medium. The media were then removed and replaced with media containing 1% formaldehyde (EM grade; tebu-bio) and crosslinked for 8 min. Crosslinking was quenched by adding glycine to a final concentration of 0.2 M. The cells were washed with ice-cold PBS, harvested in PBS, and the cell pellet was washed with PBS. The nuclear fraction was extracted by first resuspending the pellet in 10 ml of LB1 buffer (50mM HEPES-KOH [pH 7.5], 140mMNaCl, 1mMEDTA, 10% glycerol, 0.5% NP-40 or Igepal CA-630, and 0.25% Triton X-100) for 10 min at 4°C. Cells were pelleted, resuspended in 10 ml of LB2 buffer (10 mM Tris-HCL [pH 8.0], 200 mM NaCl, 1 mM EDTA, and 0.5 mM EGTA), and mixed for 5 min. Cells were pelleted and resuspended in 300 μl of LB3 buffer (10 mM Tris-HCl [pH 8], 100 mM NaCl, 1 mM EDTA, 0.5 mM EGTA, 0.1% Na-deoxycholate, and 0.5% N-lauroylsarcosine) and sonicated in a covaris sonicator for 10 min. A total of 30 μl of 10% Triton X-100 was added, and lysate was centrifuged for 10 min at 20,000 rcf to purify the debris. The supernatant was then incubated with 100 μl of magnetic beads (Life Technologies) prebound with 20 μg BRD4 antibody (Bethyl, A301-985A), and immunoprecipitation (IP) was conducted overnight in the cold room. The beads were washed ten times in 1 ml of RIPA buffer and twice in 100mM ammonium hydrogen carbonate (AMBIC) solution. DNA was eluted in elution buffer (50 mM Tris-HCl pH 8, 10 mM EDTA, and 1% SDS). Cross-links were reversed overnight at 65°C. RNA and protein were digested with 0.2 mg/mL RNase A for 2 hr followed by 0.2 mg/mL Proteinase K for 1 hr. DNA was purified with phenol chloroform extraction and ethanol precipitation. Libraries for Illumina sequencing were prepared following the Rubicon ThruPLEX-FD kit for 10-12 cycles.

RNA-seq: SUM159 and SUM159R were incubated in biological duplicates for 3, 12 and 24 hr with 500 nM of JQ1 or DMSO treatment. Total RNA was extracted using the standard

QIAGEN RNeasy kit (74106). RNA concentrations were measured and quality controlled on a Bioanalyzer, RNA-Seq libraries were made using Illumina True-Seq RNA kits using the Sciclone NGSx workstation.

All RNA-seq and ChIP-seq experiments were performed in duplicates.

Genomic data analyses

Accessing data generated in this manuscript—All ChIP-seq, Chem-seq, and RNA-seq data generated in this publication can be found online associated with GEO Publication Reference ID GSE63584 (www.ncbi.nlm.nih.gov/geo/). Supplementary Table 2 lists all sequencing datasets and their corresponding GEO GSM accession IDs.

Gene sets and annotations—All analysis was performed using RefSeq (NCBI37/HG19) human gene annotations.

RNA-seq data processing and gene expression quantification—All RNA-Seq datasets were aligned to the transcriptome using Tophat2[31] (version 2.0.11) using the Illumina igenomes NCBI37/HG19 UCSC transcriptome build retrieved from http://ccb.jhu.edu/software/tophat/igenomes.shtml. Alignments were performed using default parameters. Transcript expression quantification was performed using Cufflinks[32] (version 2.2.0) with default parameters to generate gene expression values in units of FPKM.

ChIP-seq and Chem-seq data processing—All ChIP-seq and Chem-seq datasets were aligned using Bowtie2[33] (version 2.2.1) to build version NCBI37/HG19 of the human genome or build version NCB37/MM9 of the mouse genome. Alignments were performed using the following criteria: -k 1, with all other parameters set to default. These criteria preserved only reads that mapped uniquely to the genome without any mismatches.

Calculating read density—We calculated the normalized read density of a ChIP-seq or Chem-seq dataset in any region using the Bamliquidator (version 0.9) read density calculator (https://github.com/BradnerLab/pipeline/wiki/bamliquidator). Briefly, ChIP-Seq reads aligning to the region were extended by 200bp and the density of reads per basepair (bp) was calculated. The density of reads in each region was normalized to the total number of million mapped reads producing read density in units of reads per million mapped reads per bp (rpm/bp).

Identifying ChIP-seq and Chem-seq enriched regions—We used the MACS version 1.4.2 (Model based analysis of ChIP-Seq)[34] peak finding algorithm to identify regions of ChIP-Seq enrichment over background. A p-value threshold of enrichment of 1e-9 was used for all datasets. The GEO accession number and background used for each dataset can be found in the accompanying Supplementary Table 2.

Creating heatmap representations of ChIP-seq occupancy—Heatmaps of ChIP-seq occupancy for various factors were created as described[35]. Heatmaps were created for the +/− 10kb region flanking all transcription start sites (TSS) or for the +/−10kb region flanking all TSS distal BET bromodomain bound enhancers. Each row plots a specific TSS

or enhancer region. Rows are ranked by peak occupancy of BET bromodomains as determined by Bio-JQ1 Chem-seq signal (Fig. 1d).

Correlating BRD4 and H3K27ac occupancy to Bio-JQ1—Occupancy of BRD4 and H3K27ac was correlated to Bio-JQ1 occupancy at all regions of Bio-JQ1 enrichment in SUM159 cells. Pearson correlation statistics are shown (Extended Data Fig. 3a). To quantify changes in BRD4 or H3K27ac occupancy upon JQ1 treatment, all Bio-JQ1 enriched regions were ranked in SUM159 cells and then binned (n=10). Corresponding boxplots of BRD4 or H3K27ac $\log_2$ fold change +/− JQ1 are shown for each bin (Extended Data Fig. 3b).

Mapping enhancers and super-enhancers using Bio-JQ1 occupancy or BRD4 —Enhancers and super enhancers (SEs) were mapped using the ROSE software package described[12,13] and available at (younglab.wi.mit.edu/super_enhancer_code.html). In SUM159 and SUM159R cells, Bio-JQ1 Chem-Seq enriched regions were used to map enhancers and SEs (Fig. 1f). In SUM149 cells, BRD4 ChIP-seq enriched regions were used to map enhancers and SEs (Extended Data Fig. 3). Enhancers are defined as regions of Bio-JQ1 binding not contained in promoters.

Quantifying changes in gene expression of SE proximal genes—Genes within 50kb of SE in SUM159 or SUM149 were identified and filtered for expression status (> 1 FPKM expression in any sample), and filtered to remove non poly-adenylated transcripts (e.g. microRNAs). For SUM159, $\log_2$ fold changes in gene expression at SE associated genes or all expressed genes was compared at 3, 12, and 24 hours post JQ1 treatment (Fig. 1g). For SUM149, comparisons were made at 12 hours post JQ1 treatment (Extended Data Fig. 3f). The statistical significance of differences between distributions of changes was also assessed using a Welch's two-tailed t test.

Identifying differentially expressed genes upon JQ1 treatment—To identify genes differentially regulated by JQ1 treatment in SUM159 or SUM149 cells, all genes with a > $\log_2$ fold change in expression were ordered by fold change at 24 hours +/− JQ1 for SUM159 or at 12 hours +/− JQ1 for SUM149. The $\log_2$ row median normalized fold change for each gene is displayed as a heatmap in Extended Data Fig. 3g for SUM159 and in Extended Data Fig. 3h for SUM149. For subsequent gene set and pathway analysis, SUM159 genes with consistent and statistically significantly altered expression were selected using a Welch's two-tailed t test between DMSO and JQ1 treated expression values at 12 and 24 hours. A p-value cutoff of 0.01 was applied (Extended Data Fig. 3k).

Identifying gained/lost SE between SUM159 and SUM159R—SE differential regions were defined as in Brown et al. 2014[36]. Briefly, in order to quantify changes in super-enhancers between two conditions, background subtracted ChIP-Seq signal was calculated at the set of all enhancer regions considered super in at least one condition. Gained/lost super-enhancers were determined as those with a greater than $\log_2$ fold change signal in either direction. The $\log_2$ fold change in Bio-JQ1 occupancy at all rank ordered SE containing regions is shown in Fig. 2c. SE regions were classified as either gained, conserved, or lost. Gained/lost regions were classified as those with > 1 $\log_2$ fold change in either direction. Conserved regions were classified as those with < 0.25 $\log_2$ fold change in

either direction. The $\log_2$ fold change in either BRD4 or proximal (within 50kb of region) gene expression is shown in Extended Data Fig. 5d-f.
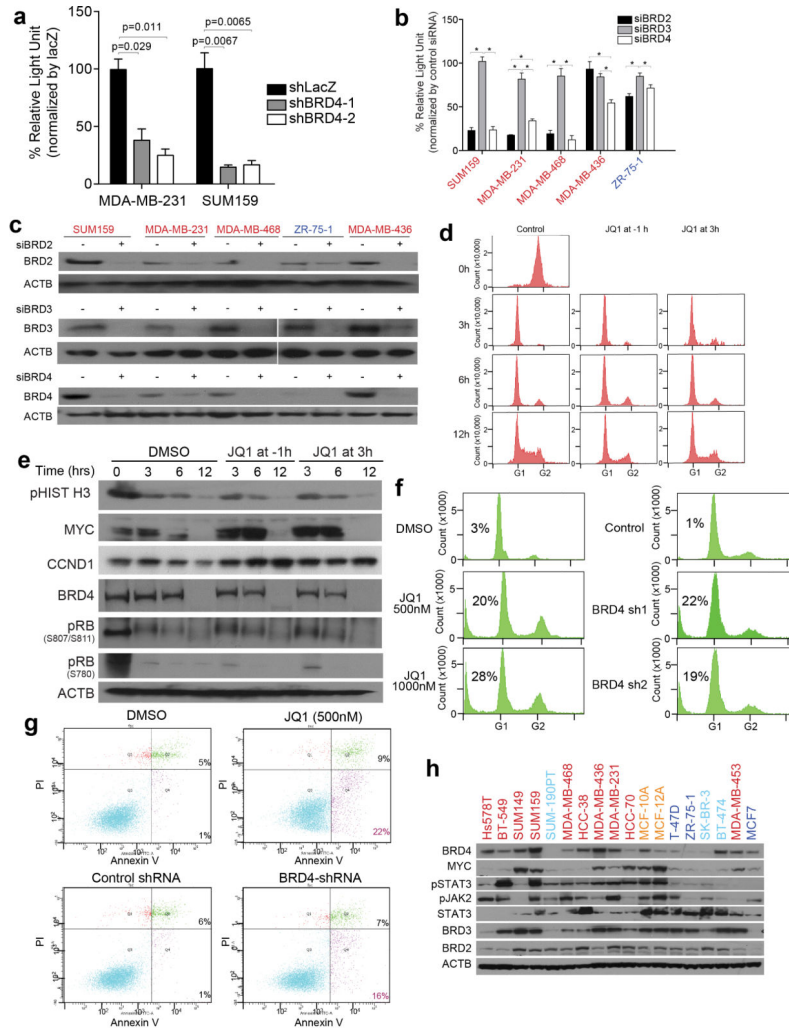
Quantifying changes in BRD4 and H3K27ac occupancy upon JQ1 treatment in either SUM159 or SUM159R cells at Bio-JQ1 regions—$\log_2$ fold changes in BRD4 or H3K27ac were quantified at Bio-JQ1 enriched regions in their respective cell line and shown in Extended Data Fig. 5c.

Quantifying changes in BRD4 and H3K27ac as a function of Bio-JQ1 or BRD4 occupancy—Bio-JQ1 enriched regions in SUM159 or BRD4 enriched regions in SUM149 were ranked by increasing levels and then distributed into 10 bins. $\log_2$ fold changes in BRD4 or H3K27ac were quantified in each bin of regions and displayed as a box plot (Extended Data Fig. 3b,c).

Quantifying changes in BRD4 occupancy upon JQ1 treatment in all TNBC—$\log_2$ fold changes in BRD4 upon JQ1 treatment were quantified at BRD4 enriched regions in each respective cell line Extended Data Fig. 6c.

All code related to genomic and transcriptome analysis can be found at https://github.com/BradnerLab/TNBC

Extended Data

Extended Data Figure 1. BET bromodomain proteins and cell growth in TNBCs

All error bars represent SD, n=3. **a**, Cellular viability of SUM159 and MDA-MB-231 cells expressing TET-inducible BRD4-targeting or lacZ shRNAs. P-values indicate statistical significance of the observed differences (paired t-test). **b**, Cellular viability four days after transfection of siRNAs targeting BET bromodomain proteins. *indicate statistical significance (paired t-test) of the marked differences as follows: SUM159: siBRD2 vs. siBRD3, p=0.002; siBRD3 vs. siBRD4, p=0.0006, MDA-MB-231: siBRD2 vs. siBRD3, p=0.006; siBRD2 vs. siBRD4, p=0.002; siBRD3 vs. siBRD4, p=0.016, MDA-MB-468: siBRD2 vs. siBRD3, p=0.0009; siBRD3 vs. siBRD4, p=0.0055, MDA-MB-436: siBRD2 vs. siBRD4, p=0.002; siBRD3 vs. siBRD4, p=0.015, ZR-75-1: siBRD2 vs. siBRD3, P=0.0169; siBRD3 vs. siBRD4, p=0.007. **c**, Immunoblot analysis of BET bromodomain proteins four days after siRNA transfection. **d**, Cell cycle profile of SUM159 cells synchronized in G2/M with 100ng/ml nocodazole followed by replating to fresh medium with DMSO or JQ1 (500nM) added at -1h or at 3h after release. Cells were collected at different time points (0, 6, 12h) after release. **e**, Immunoblot analysis of the indicated proteins at different time points
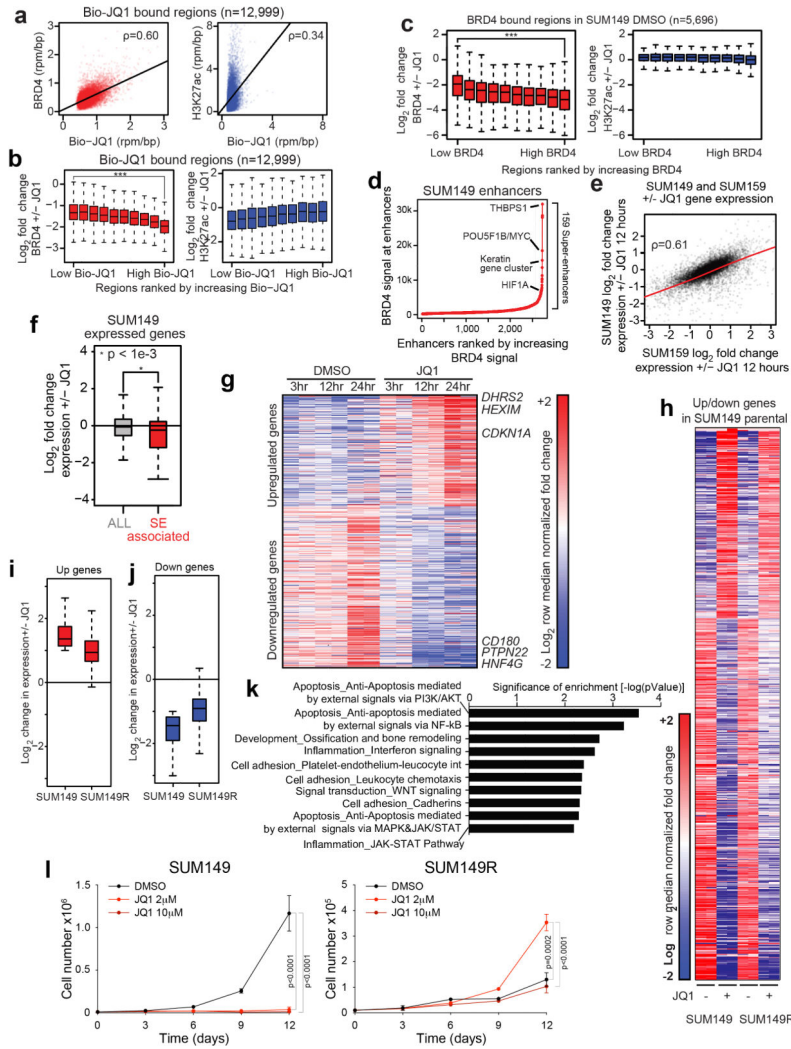
(0, 3, 6, 12h) after release of SUM159 cells synchronized with 100ng/ml nocodazole followed by replating to fresh medium with DMSO or JQ1 (500nM) added at 1hr before or 3hrs after release. **f**, Cell cycle analysis of SUM159 cells following 72 hr treatment with JQ1 (500nM) or downregulation of BRD4 using TET-inducible shRNAs. **g**, Annexin V staining of SUM159 cells following 72 hr treatment with JQ1 (500nM) downregulation of BRD4 using TET-inducible shRNAs. All error bars represent SEM. **h**, Immunoblot analysis of the indicated proteins in a panel of breast cell lines; color scheme as in panel a. For gel source data, see Supplementary Figure 1.

Extended Data Figure 2. Response to BBIs in TNBCs
a, Immunoblot analysis of the indicated proteins at different time points following JQ1 treatment (500nM) in SUM159 cells (top) and at different JQ1 doses for 24h treatment in SUM159 and MDA-MB-436 cells (bottom). **b**, Immunoblot analysis of the indicated proteins at different time points following JQ1 treatment (500nM) in SUM149, SUM159 and MDA-MB-231 cells. **c**, H&E staining of SUM159 cells after 3 days of JQ1 treatment. **d**, -Senescence β-galactosidase staining of SUM159 and MDA-MB-231 cells after 3 days of JQ1 treatment. Scale bars show 100μm. **e**, Box plots depict the weights of xenografts 30
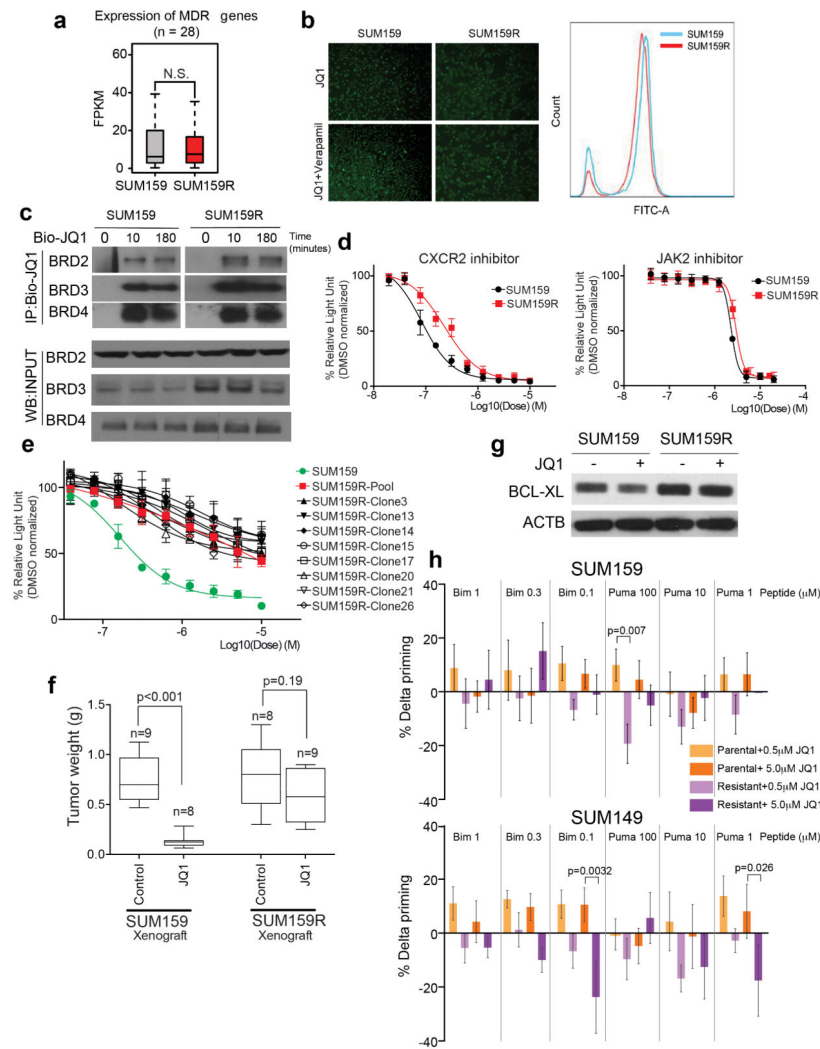
days after injection of MDA-MB-231 (2×10^6) and IDC50X (2×10^5) cells into inguinal mammary fat pads of NOG mice; n indicates the number of mice/experiment. P-values indicate statistical significance of the observed differences (unpaired t-test). Error bars represent SEM. Mice were administered JQ1 (50mg/kg, daily) or vehicle only (control) for 14 days beginning at day 16 (MDA-MB-231) or 10 (IDC50X) after injection (after tumors reached palpable size). For EL12-58X PDX, mice were implanted with pieces of tissue measuring $1\times3\times3$mm into the inguinal mammary fat pads and were administered daily JQ1 (50mg/kg) for 14 days beginning at day 21 after injection (after tumors reached palpable size). **f,** Bromodeoxyuridine (BrdU) and luminal low (Low MW CK) and basal high (High MW CK) molecular weight cytokeratin staining of EL12-58 xenograft with or without JQ1 treatment. Scale bars show 50μm. **g,** Tumor volume of SUM159 cells expressing TET-inducible BRD4-targeting shRNAs. Mice were administered doxycycline or vehicle only (control) for 39 days beginning at day 21 after injection (after tumors reached palpable size). Error bars represent SD, n=4 (shBRD4-1 experiment) and n=5 (shBRD4-2 experiment) **h,** Hematoxylin-eosine staining and immunofluorescence analysis of basal (basal cytokeratin, cytokeratin 17, pSTAT3, and CD44) and luminal (luminal cytokeratin, cytokeratin 18, and CD24) markers in SUM159 xenografts with or without JQ1 treatment. Scale bars show 100μm for H&E and 50μm for immunofluorescence, respectively. For gel source data, see Supplementary Figure 1.

Extended Data Figure 3. SUM149 JQ1 response

a, Scatter plots showing the relationship between the genomic binding of BRD4 and Bio-JQ1 (left) or H3K27ac and Bio-JQ1 (right) at all Bio-JQ1 enriched bound regions. Units of genomic occupancy are in rpm/bp. A simple linear regression is drawn in black. Pearson correlation statistics are also shown. **b,** Boxplots showing the log2 fold change in BRD4 +/− JQ1 (left) or H3K27ac +/− JQ1 (right) at Bio-JQ1 bound regions in SUM159. The 12,999 Bio-JQ1 regions are ranked by increasing Bio-JQ1 binding and divided into 10 separate bins (displayed from left to right). The statistical significance of the difference in the mean BRD4 log2 fold change between the weakest and strongest Bio-JQ1 bound region bins is shown (Welch's t-test *** p-value < 1e-10). **c,** Boxplots showing the $\log_2$ fold change in BRD4 +/− JQ1 (left) or H3K27ac +/− JQ1 (right) at BRD4 bound regions in SUM149. The 5,696 BRD4 bound regions are ranked by increasing background subtracted BRD4 binding and divided into 10 separate bins (displayed from left to right). The statistical significance of the difference in the mean BRD4 $\log_2$ fold change between the weakest and strongest BRD4 bound region bins is shown (Welch's t-test *** p-value < 1e-10). **d,** Ranked plots of enhancers defined in untreated SUM149 cells ranked by increasing BRD4 signal (units
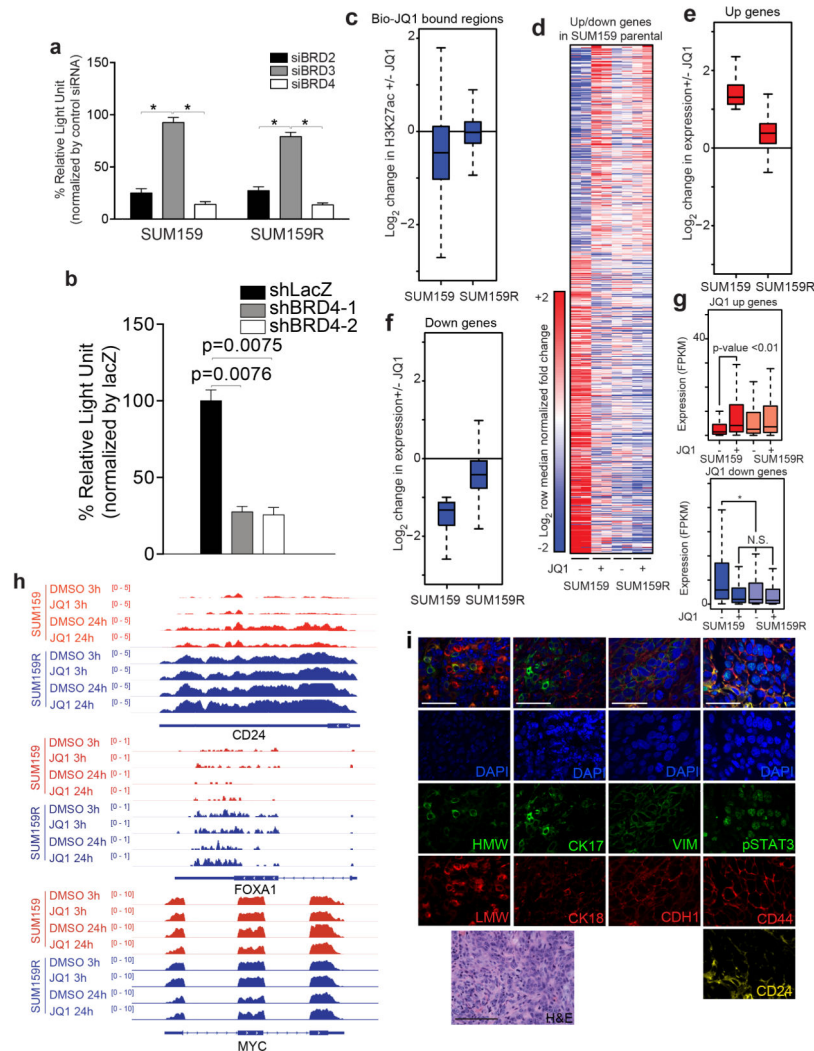
rpm). Enhancers are defined as regions of BRD4 binding not contained in promoters. The cutoff discriminating typical from super-enhancers is shown as a dashed gray line. Enhancers associated with TNBC characteristic genes are highlighted. **e,** Scatter plots showing the relationship between the $\log_2$ fold change in gene expression upon 12hr JQ1 treatment in SUM149 (y-axis) and SUM159 (x-axis). A simple linear regression is drawn in red. The Pearson correlation statistic is also shown. **f**, Boxplots showing the $\log_2$ fold change in expression relative to DMSO control of either all active genes or super-enhancer (SE) associated upon 12hr JQ1 treatment. The statistical significance of the difference in expression change between all active genes and super-enhancer associated genes is shown by a Welch's t-test * p-value < 1e-3). **g,** Heatmap showing the expression of genes that are up or down regulated by JQ1 versus DMSO after 24 hours treatment. Each row shows the expression of a single gene in either DMSO or JQ1 treated cells at 3, 12, and 24 hours after treatment. Expression values are colored according to fold change relative to the median for each row. Genes are ordered by fold change +/− JQ1 24 hours after treatment. **h,** Heatmap showing the expression of genes that are up or down regulated by JQ1 versus DMSO after 12 hours treatment in SUM149 and SUM149R cells. Each row shows the expression of a single gene in either DMSO or JQ1 treated cells at 12 hours after treatment. Expression values are colored according to fold change relative to the median for each row. Genes are ordered by fold change +/− JQ1 12 hours after treatment in SUM149 cells. **i,j,** Boxplots showing the $\log_2$ fold change in expression at genes that are up (**i**) or down (**j**) regulated by JQ1 versus DMSO after 12 hours of treatment in parental SUM149 cells. $\log_2$ fold change in expression is shown for either parental SUM149 (left) or resistant SUM149R (right) cells. **k,** Top signaling pathways affected by JQ1-induced gene expression changes in SUM159 cells. **l,** Viable cell numbers of SUM149 (left) and SUM149R (right) treated with different doses of JQ1 (2μM, 10μM). Error bars represent SD, n=3. P-values indicate statistical significance of the observed differences (two-way ANOVA with Bonferroni multiple comparison correction).

Extended Data Figure 4. Characterization of SUM159R cells

a, Expression of ABC transporters in SUM159 and SUM159R cells. The expression of 29 ABC transporters was analyzed based on RNA-seq data on the two cell lines. **b**, Assay for MDR (multi drug resistance) pumps in SUM159 and SUM159R cells treated with JQ1 alone or together with verapamil based on microscopic examination (left) and FACS (right) of cells labeled with fluorescent MDR substrate. **c**, Immunoprecipitation analysis of Biotinylated JQ1 (Bio-JQ1) in SUM159 and SUM159R cells with JQ1 treatment at different time points following immunoblot for the indicated proteins. **d,** Cellular viability of SUM159 and SUM159R cells treated with CXCR2 and JAK2 inhibitors. Error bars represent SD, n=3. **e,** Cellular viability of SUM159, and pool and single cell clones of SUM159R cells treated with different doses of JQ1. Error bars represent SD, n=3. **f,** Tumor weight of xenografts derived from SUM159 and SUM159R cells. Mice were administered JQ1 for 14 (SUM159) and 30 (SUM159R) days beginning at day 14 and 26, respectively, after injection. P-values indicate statistical significance of the observed differences (unpaired t-test). Error bars represent SEM. **g,** Immunoblot analysis of BCL-XL expression in SUM159 and SUM159R cells before and after JQ1 3h treatment (500nM). **h,** Dynamic BH3
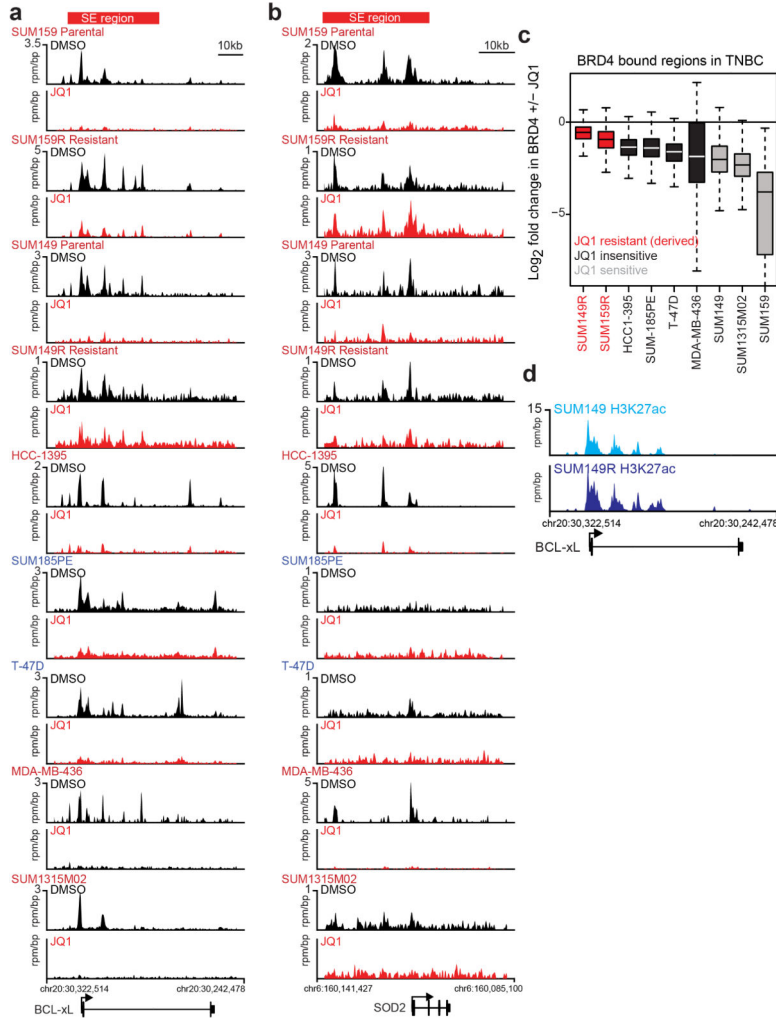
profiling reveals inverse apoptotic response to JQ1 in SUM149R and SUM159R cells. In parental lines JQ1 increases priming relative to untreated cells indicating an increase in apoptotic propensity. In resistant lines JQ1 reduces priming indicating greater resistance to apoptosis relative to untreated cells. P-values indicate statistical significance of the observed differences (two-way ANOVA). Error bars represent SEM, n=5. For gel source data, see Supplementary Figure 1.
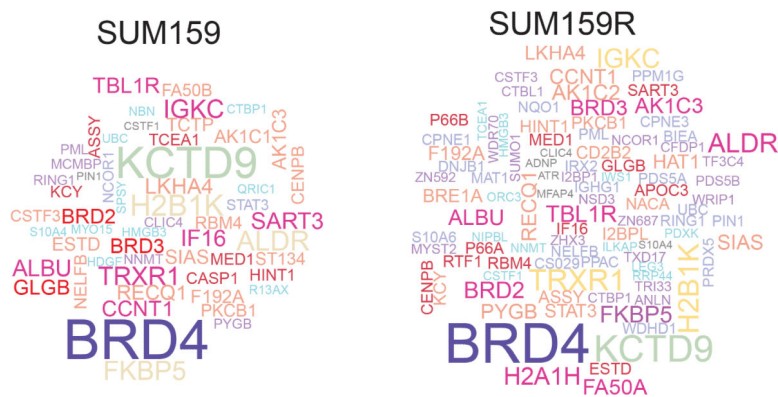

Extended Data Figure 5. BRD4 binding in SUM159R cells

a, Cellular viability of SUM159 and SUM159R cells transfected with siRNAs targeting bromodomain proteins. *indicate statistical significance (paired t-test) of the marked differences as follows: SUM159: siBRD2 vs. siBRD3, p=0.013, siBRD3 vs. siBRD4, p=0.0154 and SUM159R: siBRD2 vs. siBRD3, p=0.0159, siBRD2 vs. siBRD4, p=0.0048; siBRD3 vs. siBRD4, p=0.0068. **b**, Cellular viability of SUM159R cells expressing TET-inducible BRD4-targeting or lacZ shRNAs. All error bars represent SEM. P-values indicate statistical significance of the observed differences (unpaired t-test). **c,** Boxplot showing the log2 fold change in H3K27ac genomic occupancy at regions bound by Bio-JQ1 in parental
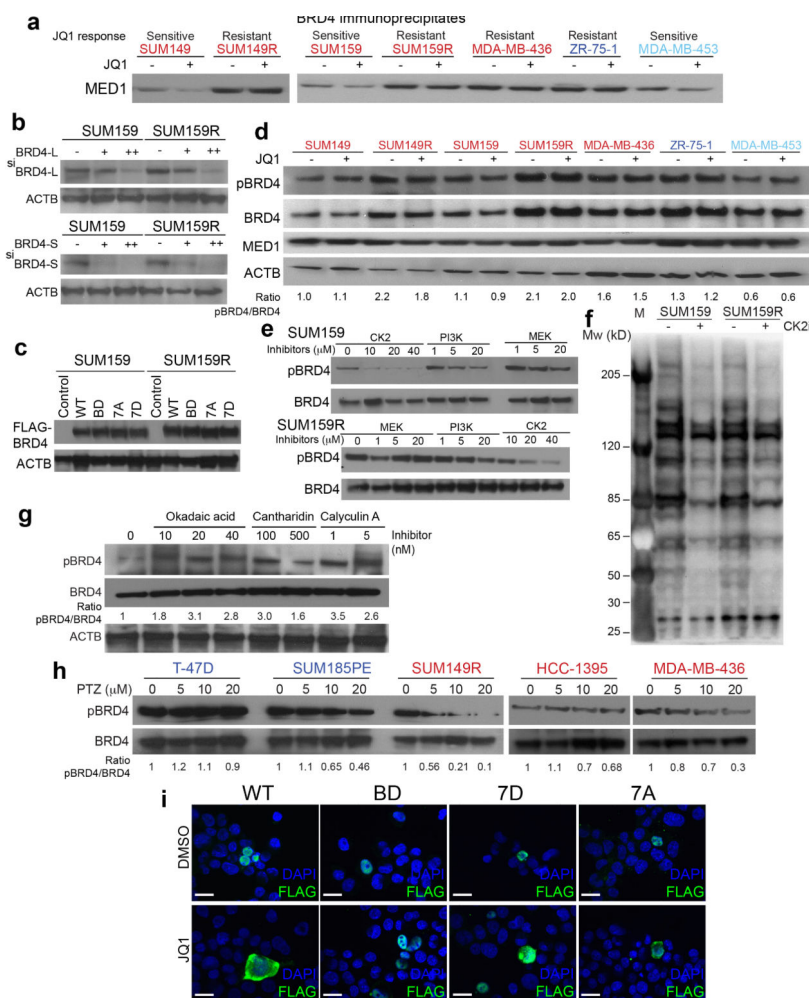
SUM159 or resistant SUM159R cells. **d,** Heatmap showing the expression of genes that are up or down regulated by JQ1 versus DMSO after 24 hours treatment in parental SUM159 cells. Each row shows the expression of a single gene in either DMSO or JQ1 treated cells at 24 hours after treatment in SUM159 cells (left four columns) or SUM159R cells (right four columns). Expression values are colored according to fold change relative to the median for each row. Genes are ordered by fold change +/− JQ1 24 hours after treatment. **e,f,** Boxplots showing the log2 fold change in expression at genes that are up (**e**) or down (**f**) regulated by JQ1 versus DMSO after 24 hours of treatment in parental SUM159 cells. Log2 fold change in expression is shown for either parental SUM159 or resistant SUM159R cells. **g,** Boxplots showing expression of genes that are up or down regulated by JQ1 versus DMSO after 24 hours of treatment in parental SUM159 cells. Expression is shown in DMSO and JQ1-treated conditions in units of FPKM for either parental SUM159 (left) or resistant SUM159R (right) cells. The statistical significance of the difference between gene expression distributions for SUM159 DMSO and JQ1 treated cells is shown (p <0.01). The difference between all other distributions are considered non significant (N.S). The statistical significance of the difference between SUM159 DMSO gene expression distribution and all other distributions is shown (* p-value < 1e-3). The difference between all other distributions are considered non significant. **h,** Examples of luminal and basal cell-specific genes, and MYC in SUM159 and SUM159R cells. RNA-seq tracks are shown. **i,** H&E staining and immunofluorescence analysis of luminal (CK18 and LMW) and basal (CK17 and HMW) cytokeratins and luminal (VIM and CD24) and basal (CDH1, CD44, and pSTAT3) cell markers in SUM159R xenografts. All error bars represent SEM. Scale bars show 100μm for H&E and 50μm for IF respectively.

Extended Data Figure 6. JQ1 response in other breast cancer cell lines
a,b, Gene tracks depicting BRD4 + DMSO and BRD4 + JQ1 in multiple TNBC cells at the *BCL-xL* (a) or *SOD2* (b) gene loci. The x-axis shows position along the chromosome with gene structures drawn below. The y-axis shows genomic occupancy in units of rpm/bp. The *BCL-xL* and *SOD2* super-enhancers are shown as a red bar at the top. **c,** Box plots showing the log₂ fold change in BRD4 occupancy +/− JQ1 for all BRD4 bound regions in each cell line for multiple TNBC. Cell lines are ordered by their JQ1 (IC50) and colored by their sensitivity. **d,** Gene tracks depicting H3K27AC occupancy at the *BCL-xL* locus in SUM149 parental (top, light blue) or SUM149R resistant (bottom, dark blue) cells. The x-axis shows position along the chromosome with gene structures drawn below. The y-axis shows genomic occupancy in units of rpm/bp. All error bars represent SEM.
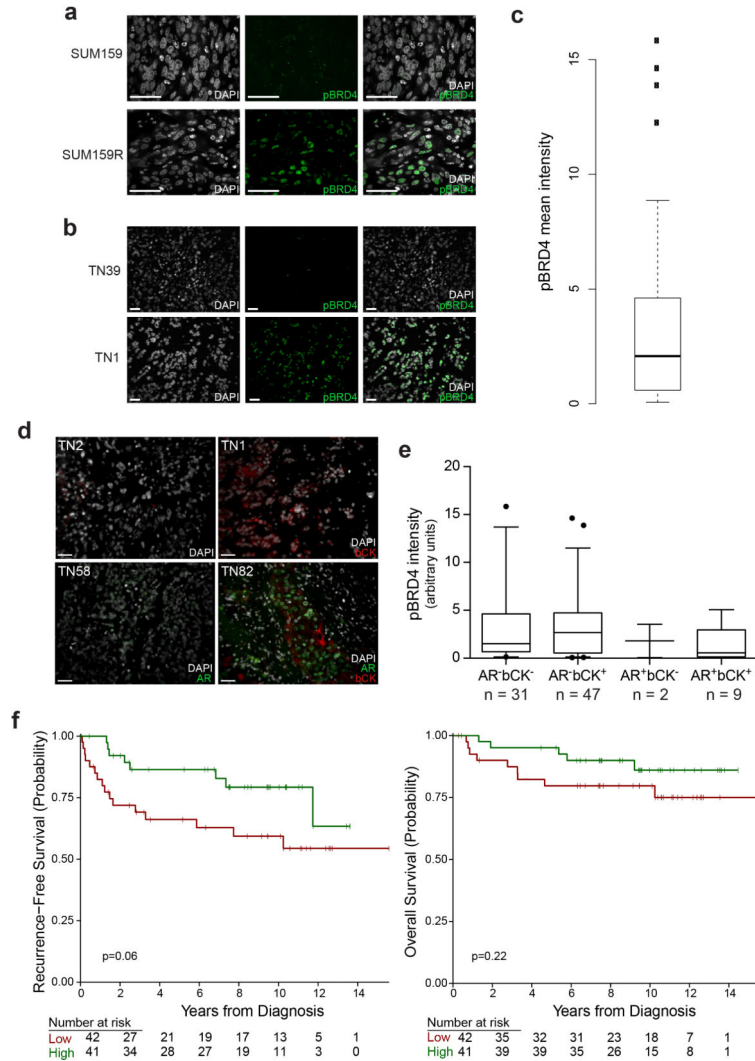
Extended Data Figure 7.
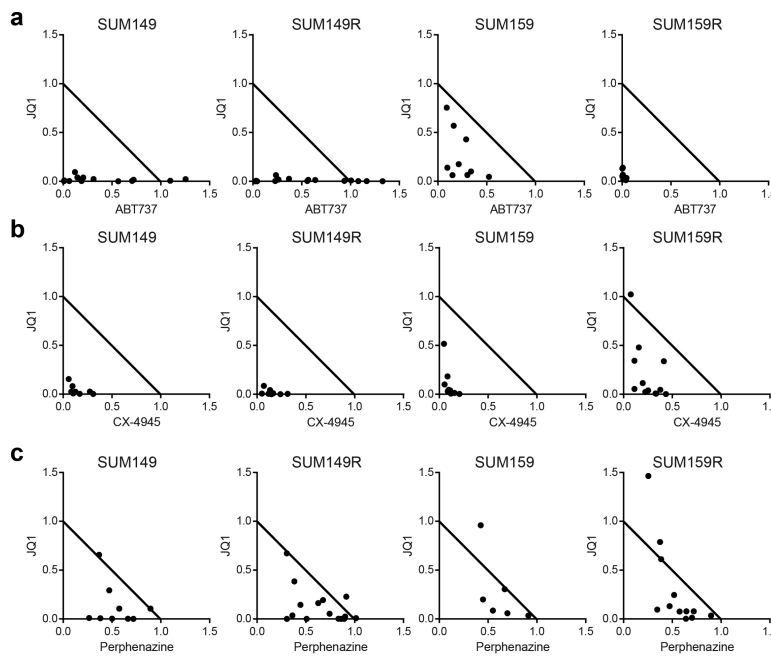Word clouds depicting BRD4-associated proteins identified in RIME analysis.

Extended Data Figure 8. Mechanism of BBI-resistance
a, Immunoblot analysis of BRD4 immunoprecipitates for MED1 in the indicated cell lines with or without JQ1 treatment (5uM, 3h). **b,** Immunoblot analysis of long (BRD4L) and short (BRD4S) forms of BRD4 after transfection of siRNAs. **c,** Immunoblot analysis of the

indicated exogenously expressed FLAG-tagged BRD4 proteins in SUM159 and SUM159R cells. **d,** Immunoblot analysis of phospho-BRD4 (pBRD4) and BRD4 in SUM159 and SUM159R cells treated with the indicated doses of CK2, PI3K, and MEK inhibitors for 2hrs. **e,** Immunoblot analysis of pBRD4, BRD4, MED1 and ACTB in the indicated cell lines with or without JQ1 treatment. **f,** Immunoblot analysis of CK2 substrates in SUM159 and SUM159R cells following CK2 inhibitor (CX-4945, 10μM) 3h treatment. **g,** Immunoblot analysis of pBRD4 and BRD4 in SUM149 cell line treated with different doses of the indicated PP2A inhibitors for 3hrs. ACTB was used as loading control. **h,** Immunoblot analysis of pBRD4 and BRD4 in the indicated cell lines treated with different doses of phenothiazine for 6hrs. **i,** Immunofluorescence analysis of exogenous FLAG-tagged BRD4 proteins (WT, BD, 7D and 7A) in SUM159 cells with or without JQ1 treatment (5μM, 3hrs). Scale bars show 20μm. For gel source data, see Supplementary Figure 1.

Extended Data Figure 9.
Phospho-BRD4 levels in xenografts and primary TNBC samples. **a,** Immunofluorescence analysis of phospho-BRD4 (pBRD4) in SUM159 parental and SUM159R xenografts

showing that resistance is associated with higher pBRD4 levels. **b,** Examples of pBRD4 immunofluorescence in patient tumors depicting variability among different TNBC samples. Scale bars show 50μm. **c.** Mean intensity of phospho-BRD4 (pBRD4) in tissue samples from 83 patients with early-stage triple negative breast cancer (TNBC). **d,** Examples of AR and basal cytokeratin (bCK, HMW CK) immunofluorescence in TNBC samples. Scale bars show 50μm. **e**, Box plot depicting pBRD4 signal intensity in TNBCs tumors with the indicated AR and bCK expression patterns. None of the differences among groups were significant (ANOVA test – p = 0.5413 and Dunnett's multiple comparisons test - not significant). **f**, Kaplan-Meier estimates of disease-free survival (DFS) and overall survival (OS) in TNBC subgroups using a median-split of pBRD4 intensity. Disease outcomes were evaluated in 83 of 89 TMA samples. Patients with low pBRD4 had a worse overall prognosis with a five-year RFS of 66.2% (95% CI 52.7-83.1%), compared to an RFS of 86.4% (95% CI 76.0-98.3%) among patients with high pBRD4 (HR=2.3, 95%CI 0.98-5.4, p=0.06). However, with this small sample size this difference did not reach statistical significance, nor did a ratiometric (2-fold) consideration of pBRD4 status and overall survival (HR=2.0, 95%CI 0.67-5.9, p=0.22).

Extended Data Figure 10.
Overcoming BBI-resistance. a-c, Synergy studies of JQ1 with ABT737 (BCL-xl and BCL-2 inhibitor) (a), CX-4945 (CK2 inhibitor) (b) and Perphenazine (PP2A activator) (c). Points represent paired values of drug concentrations assessed for synergism. The diagonal line signifies drug additivity. Points above the line represent antagonistic drug combinations, and those below the line represent synergistic drug combinations.

Supplementary Material

Refer to Web version on PubMed Central for supplementary material.

REFERENCES

1. Vaz-Luis I, et al. Outcomes by tumor subtype and treatment pattern in women with small, node-negative breast cancer: a multi-institutional study. J Clin Oncol. 2014; 32:2142–2150. [PubMed: 24888816]

2. Lehmann BD, et al. Identification of human triple-negative breast cancer subtypes and preclinical models for selection of targeted therapies. J Clin Invest. 2011; 121

3. Metzger-Filho O, et al. Dissecting the heterogeneity of triple-negative breast cancer. J Clin Oncol. 2012; 30:1879–1887. [PubMed: 22454417]

4. Puissant A, et al. Targeting MYCN in neuroblastoma by BET bromodomain inhibition. Cancer Discov. 2013; 3:308–323. [PubMed: 23430699]

5. Delmore JE, et al. BET bromodomain inhibition as a therapeutic strategy to target c-Myc. Cell. 2011; 146:904–917. [PubMed: 21889194]

6. Filippakopoulos P, et al. Selective inhibition of BET bromodomains. Nature. 2010; 468:1067–1073. [PubMed: 20871596]

7. Belkina AC, Denis GV. BET domain co-regulators in obesity, inflammation and cancer. Nat Rev Cancer. 2012; 12:465–477. [PubMed: 22722403]

8. Chapuy B, et al. Discovery and characterization of super-enhancer-associated dependencies in diffuse large B cell lymphoma. Cancer Cell. 2013; 24:777–790. [PubMed: 24332044]

9. Hnisz D, et al. Super-enhancers in the control of cell identity and disease. Cell. 2013; 155:934–947. [PubMed: 24119843]

10. Burstein MD, et al. Comprehensive genomic analysis identifies novel subtypes and targets of triple-negative breast cancer. Clin Cancer Res. 2015; 21:1688–1698. [PubMed: 25208879]

11. Anders L, et al. Genome-wide localization of small molecules. Nat Biotechnol. 2014; 32:92–96. [PubMed: 24336317]

12. Loven J, et al. Selective inhibition of tumor oncogenes by disruption of super-enhancers. Cell. 2013; 153:320–334. [PubMed: 23582323]

13. Whyte WA, et al. Master transcription factors and mediator establish super-enhancers at key cell identity genes. Cell. 2013; 153:307–319. [PubMed: 23582322]

14. Hayashi H, et al. The OCT4 pseudogene POU5F1B is amplified and promotes an aggressive phenotype in gastric cancer. Oncogene. 2013

15. Semenza GL. HIF-1 mediates metabolic responses to intratumoral hypoxia and oncogenic mutations. J Clin Invest. 2013; 123:3664–3671. [PubMed: 23999440]

16. Bessarabova M, et al. Functional synergies yet distinct modulators affected by genetic alterations in common human cancers. Cancer Res. 2011; 71:3471–3481. [PubMed: 21398405]

17. Marotta LL, et al. The JAK2/STAT3 signaling pathway is required for growth of CD44CD24 stem cell-like breast cancer cells in human tumors. J Clin Invest. 2011; 121:2723–2735. [PubMed: 21633165]

18. Ryan J, Letai A. BH3 profiling in whole cells by fluorimeter or FACS. Methods. 2013; 61:156–164. [PubMed: 23607990]

19. Montero J, et al. Drug-induced death signaling strategy rapidly predicts cancer response to chemotherapy. Cell. 2015; 160:977–989. [PubMed: 25723171]

20. Mohammed H, et al. Endogenous purification reveals GREB1 as a key estrogen receptor regulatory factor. Cell reports. 2013; 3:342–349. [PubMed: 23403292]

21. Wu SY, Lee AY, Lai HT, Zhang H, Chiang CM. Phospho switch triggers Brd4 chromatin binding and activator recruitment for gene-specific targeting. Mol Cell. 2013; 49:843–857. [PubMed: 23317504]

22. Rincon R, et al. PP2A inhibition determines poor outcome and doxorubicin resistance in early breast cancer and its activation shows promising therapeutic effects. Oncotarget. 2015; 6:4299–4314. [PubMed: 25726524]

23. Westermarck J, Hahn WC. Multiple pathways regulated by the tumor suppressor PP2A in transformation. Trends Mol Med. 2008; 14:152–160. [PubMed: 18329957]

24. Eichhorn PJ, Creyghton MP, Bernards R. Protein phosphatase 2A regulatory subunits and cancer. Biochim Biophys Acta. 2009; 1795:1–15. [PubMed: 18588945]

25. Gutierrez A, et al. Phenothiazines induce PP2A-mediated apoptosis in T cell acute lymphoblastic leukemia. J Clin Invest. 2014; 124:644–655. [PubMed: 24401270]

26. Rathert P, et al. Transcriptional plasticity promotes primary and acquired resistance to BET inhibition. Nature. 2015

27. Fong CY, et al. BET inhibitor resistance emerges from leukaemia stem cells. Nature. 2015

28. Chou TC, Talalay P. Quantitative analysis of dose-effect relationships: the combined effects of multiple drugs or enzyme inhibitors. Advances in enzyme regulation. 1984; 22:27–55. [PubMed: 6382953]

29. Choudhury S, et al. Molecular Profiling of Human Mammary Gland Links Breast Cancer Risk to a p27(+) Cell Population with Progenitor Characteristics. Cell stem cell. 2013; 13:117–130. [PubMed: 23770079]

30. Mellacheruvu D, et al. The CRAPome: a contaminant repository for affinity purification-mass spectrometry data. Nat Methods. 2013; 10:730–736. [PubMed: 23921808]

31. Trapnell C, Pachter L, Salzberg SL. TopHat: discovering splice junctions with RNA-Seq. Bioinformatics. 2009; 25:1105–1111. [PubMed: 19289445]

32. Trapnell C, et al. Transcript assembly and quantification by RNA-Seq reveals unannotated transcripts and isoform switching during cell differentiation. Nat Biotechnol. 2010; 28:511–515. [PubMed: 20436464]

33. Langmead B, Trapnell C, Pop M, Salzberg SL. Ultrafast and memory-efficient alignment of short DNA sequences to the human genome. Genome Biol. 2009; 10:R25. [PubMed: 19261174]

34. Zhang Y, et al. Model-based analysis of ChIP-Seq (MACS). Genome Biol. 2008; 9:R137. [PubMed: 18798982]

35. Lin CY, et al. Transcriptional amplification in tumor cells with elevated c-Myc. Cell. 2012; 151:56–67. [PubMed: 23021215]

36. Brown JD, et al. NF-kappaB Directs Dynamic Super Enhancer Formation in Inflammation and Atherogenesis. Mol Cell. 2014; 56:219–231. [PubMed: 25263595]
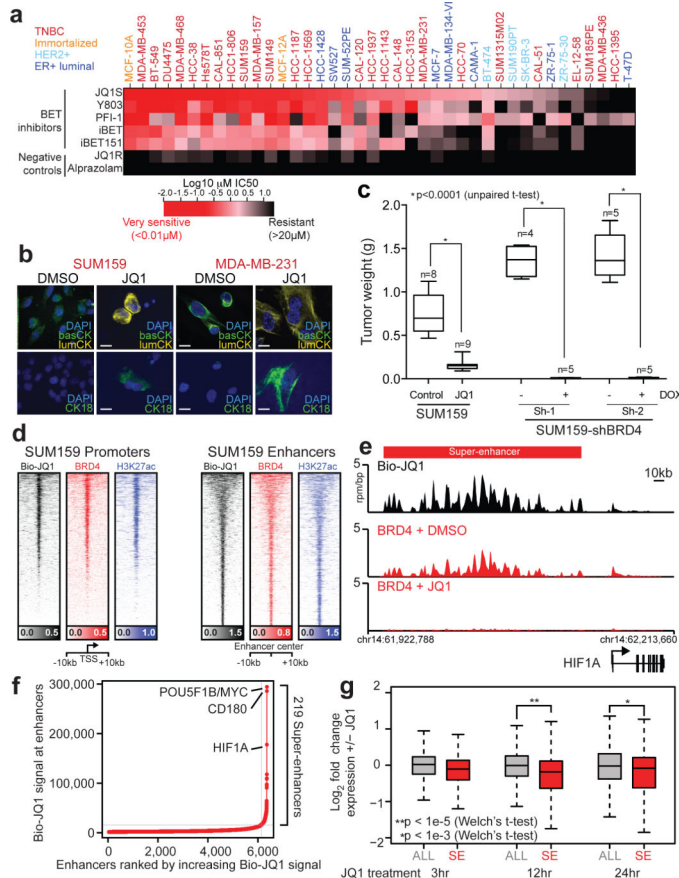
Figure 1. Response to BBIs in breast cancer

a, Heatmap of mean IC50s of BBIs and inactive analogues in breast cell lines. Error bars represent SEM. **b**, Immunofluorescence of basal (basCK) and luminal (lumCK and CK18) cytokeratins in TNBC lines. Scale bars 20µm. **c**, Box plots depicting xenograft weights; n indicates the number of mice/experiment. **d**, Heatmap showing biotinylated JQ1 (Bio-JQ1), BRD4, and H3K27ac binding at transcription start site (TSS) and Bio-JQ1-bound enhancer regions. Each row represents a single genomic region (+/− 10kb) from TSS or enhancer center. Genomic occupancy is shaded by binding intensity in units of reads per million per base pair (rpm/bp). **e**, Gene tracks depicting Bio-JQ1 and BRD4 −/+ JQ1 in SUM159 cells at the *HIF1A* locus. x-axis: chromosome position with gene structures below, y-axis: genomic occupancy in units of rpm/bp, red bar: *HIF1A* super-enhancer. **f**, Plot of enhancers defined in untreated SUM159 cells ranked by increasing Bio-JQ1 signal (units rpm). Gray line marks cutoff discriminating typical from super-enhancers. **g**, Boxplots showing the $\log_2$ fold change in expression relative to control of either all active or super-enhancer (SE) associated genes upon JQ1 treatment.
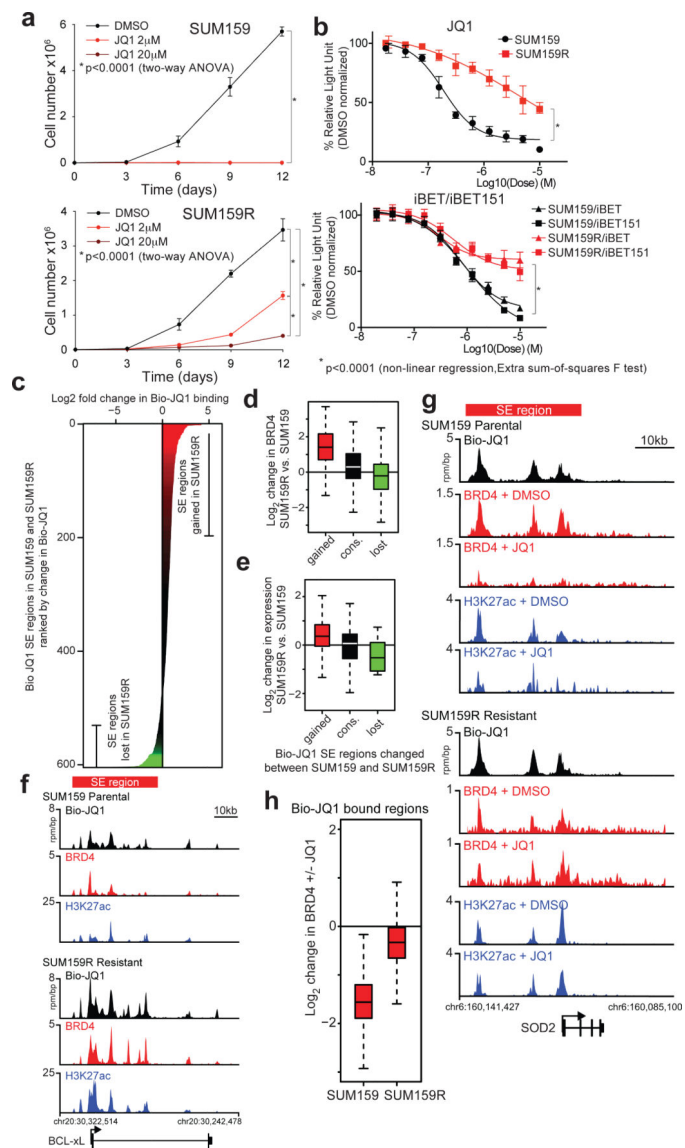
Figure 2. Acquired BBI-resistance in TNBC

All error bars represent SD, n=3. **a,** Viable cell numbers after JQ1 treatment. **b**, Cellular viability after treatment with BBIs. **c**, Genomic regions containing a super-enhancer in SUM159 or SUM159R cells ranked by $\log_2$ change in Bio-JQ1 genomic binding signal. X-axis: $\log_2$ fold change in Bio-JQ1 signal colored by intensity of change. **d, e**, Boxplot showing the $\log_2$ fold change in BRD4 genomic occupancy (**d**) and gene expression (**e**) at regions with gained, conserved, or lost Bio-JQ1 binding in SUM159R vs.. SUM159 cells. **f,g,** Gene tracks depicting Bio-JQ1, BRD4, and H3K27ac at the *BCL-xL* (**f**) and *SOD2* (**g**) locus. The x-axis shows position along the chromosome with gene structures drawn below. The y-axis shows genomic occupancy in units of rpm/bp. **h,** Boxplot showing the $\log_2$ fold change in BRD4 genomic occupancy at regions bound by Bio-JQ1.
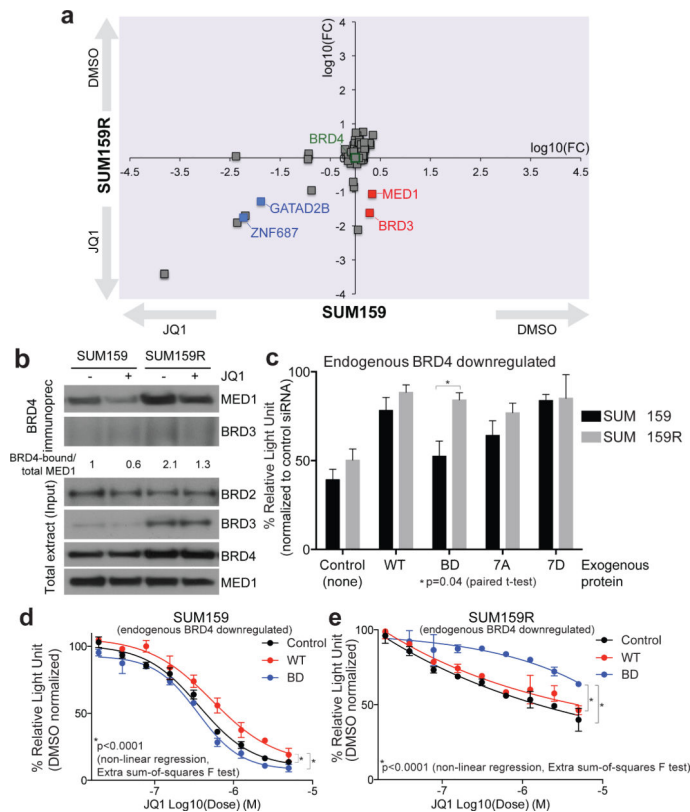
Figure 3. Mechanism of BBI-resistance in TNBCs

All error bars represent SD, n=3. **a**, Plot depicting changes in BRD4-associated proteins in SUM159 and SUM159R cells following JQ1 treatment based on SILAC RIME. The axes represent log10 of fold change (FC). **b**, Immunoblot analysis of BRD4 immunoprecipitates and total cell lysates in SUM159 and SUM159R cells. For gel source data, see Supplementary Figure 1. **c**, Cellular viability of SUM159 and SUM159R cells expressing exogenous WT, BDmut, 7A and 7D mutant BRD4 with concomitant knock-down of endogenous BRD4. **d, e,** Sensitivity of SUM159 (**d**) and SUM159R (**e**) cells expressing exogenous WT or BDmut BRD4 to JQ1 with concomitant knock-down of endogenous BRD4.
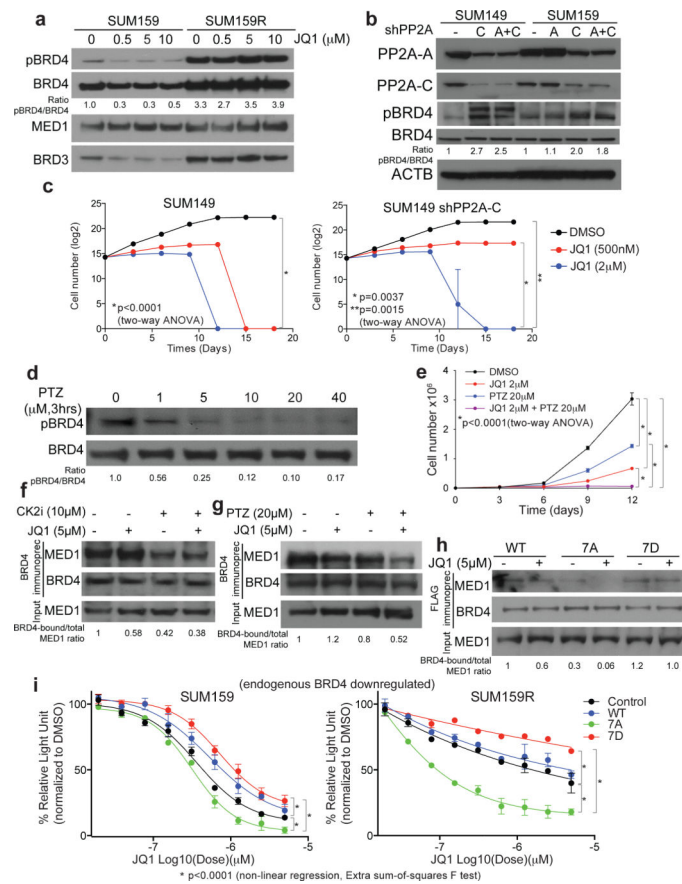
Figure 4. Regulation and relevance of BRD4 phosphorylation
All error bars represent SD, n=3. **a,** Immunoblot for the indicated proteins following JQ1 treatment. **b,** Immunoblot for the indicated proteins after knock-down of PP2A A or C or both subunits. **c,** Viable cell numbers of JQ1-treated control and shPP2A-C expressing SUM149 cells. **d,** Immunoblot of pBRD4 and BRD4 in SUM159R cells following phenothiazine (PTZ) treatment. **e,** Viable cell numbers of SUM159R cells treated with JQ1, phenothiazine or both compounds. **f,g** Immunoblot of BRD4 immunoprecipitates and total cell lysates of SUM159R cells after 3hrs treatment with JQ1 and CK2i (**f**) and JQ1 and PTZ (**g**). **h,** Immunoblot of FLAG-BRD4 (WT or mutant) immunoprecipitates and total cell lysates after 3hrs treatment with JQ1. **i,** JQ1 sensitivity of SUM159 and SUM159R cells expressing exogenous WT or mutant (7A, 7D) BRD4. For gel source data, see Supplementary Figure 1.